Surfactant-laden bubble bursting: Dynamics of capillary waves and Worthington jet at large Bond number

P. Pico [1], L. Kahouadji [1,*], S. Shin [2], J. Chergui [3], D. Juric [3,4] and O. K. Matar [1]

[1]*Department of Chemical Engineering, Imperial College London, South Kensington Campus, London SW7 2AZ, United Kingdom*
[2]*Department of Mechanical and System Design Engineering, Hongik University, Seoul 04066, Korea*
[3]*Université Paris Saclay, Centre National de la Recherche Scientifique (CNRS), Laboratoire Interdisciplinaire des Sciences du Numérique (LISN), 91400 Orsay, France*
[4]*Department of Applied Mathematics and Theoretical Physics, University of Cambridge, Cambridge CB3 0WA, United Kingdom*

We present a numerical study of the main substages preceding aerosol formation via bursting bubbles: capillary wave propagation along the bubble, convergence at the bubble's apex, and the ascent of a Worthington jet and its breakup to release liquid drops. We focus on two crucial yet overlooked aspects of the system: the presence of surface-active agents and dynamics driven by non-negligible gravitational effects, quantified by the Bond number. Our results propose a mechanism explaining capillary wave retardation in the presence of surfactants, involving the transition from bi- to unidirectional Marangoni stresses, which pull the interface upwards, countering the motion of the waves. We also quantitatively elucidate the variable nature of the waves' velocity with various surfactant parameters, including surfactant solubility and elasticity, a departure from the constant behavior well documented in clean interfaces.

I. INTRODUCTION

Aerosol droplets, arising from the bursting of bubbles at a liquid-gas interface, hold a crucial position at the confluence of diverse natural phenomena, industrial applications, and daily activities. Consider, for instance, the effervescence in sparkling drinks like champagne, where the bubbles that nucleate at the glass walls and eventually burst at the surface release the aromas experienced by the human senses [1]. In atmospheric physics, marine aerosol plays a pivotal role in governing the overall mass and heat exchange process between the oceans and the atmosphere. This stems from the liberated liquid drops, formed from an estimated 10^{18}–10^{20} bursting bubbles per second across the oceans [2] and capable of transporting an array of often surface-active substances, including salts, dissolved gases, biological material (e.g., harmful pathogens), microplastics, and toxic chemicals. Spanning a broad size range, from a few nanometers to several millimeters [3], marine aerosol actively participates in atmospheric chemical reactions, acts as nuclei for cloud and fog condensation, and can influence cyclone intensity [3,4].

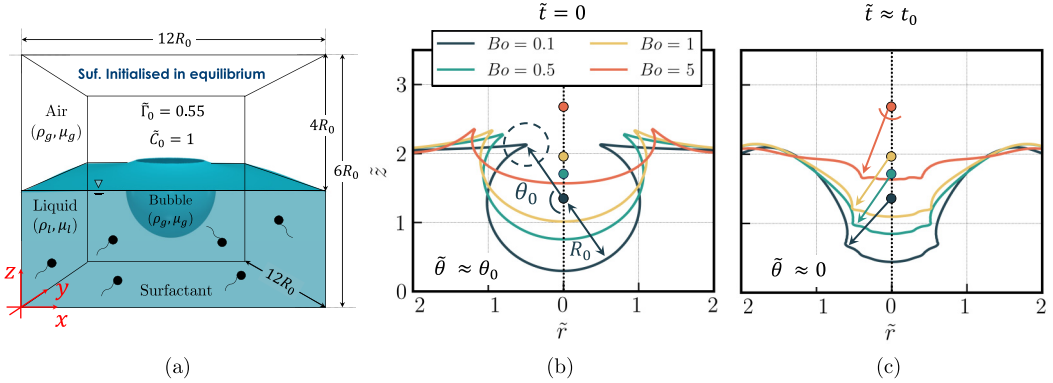*Contact author: l.kahouadji@imperial.ac.uk

FIG. 1. Three-dimensional (3D) computational domain in a Cartesian coordinate system $\mathbf{x} = (x, y, z)$ and initial bubble shapes. A radial coordinate is defined as $r = \sqrt{(x - x_0)^2 + (y - y_0)^2}$, where x_0 and y_0 correspond to the domain's center point: (a) schematic representation of the simulated domain, showcasing an equilibrated initial bubble immersed in a liquid pool with initial surfactant concentration $\tilde{C}_0$ and interfacial concentration $\tilde{\Gamma}_0$ (not to scale); (b) two-dimensional (2D) projection in an *x-z* plane of initial ($\tilde{t} = 0$) bubble shape for different Bo; and (c) representation of an instant approaching cavity collapse ($\tilde{t} \approx t_0$) at the bubble apex, where $\tilde{\theta} \approx 0$. The points located at $\tilde{r} = 0$ in (b) and (c) mark the center of each bubble, from which the angle of the dominant capillary wave is measured [8]. The dashed circle highlights the high-curvature region connecting the cavity to the liquid pool.

The aforementioned significance of aerosol droplets generated via bursting of bubbles has made the system a notable problem within the realm of fluid mechanics, witnessing substantial advancements since the latter half of the previous century. In the absence of contaminants, the dynamics of an isolated bursting bubble of radius R_0 are governed by the interplay among buoyancy, surface tension, and viscosity, quantified by the Laplace number, $\mathrm{La} = \rho_l \sigma_s R_0 / \mu_l^2$ (which can also be defined as Ohnesorge number, $\mathrm{Oh} = \mathrm{La}^{-1/2}$) and the Bond number, $\mathrm{Bo} = \rho_l g R_0^2 / \sigma_s$. In these equations, ρ, μ, σ_s, and g correspond to density, viscosity, surface tension, and gravity, respectively, and the subscript l represents the continuous liquid phase. A typical initiation of an isolated bursting event involves a spherical bubble rising in a liquid medium, reaching the surface, and creating a thin liquid film [characterized by a length scale $\delta / R_0 \sim O(10^{-6})$–$O(10^{-3})$] that separates the bubble from the atmosphere. In situations where $R_0 < l_c$, l_c being the capillary length scale [5,6], this thin film undergoes drainage at an exponential or algebraic rate [7] until its ultimate collapse, triggering the development of capillary waves that propagate on two fronts: across the bubble's domain, and away from the cavity [see Fig. 1(a)]. The bubble's capillary waves converge at the cavity's origin and induce a far-field flow which accelerates the liquid phase towards the axis of symmetry [9] and causes a reversal of the bubble-liquid interface, bringing about the ejection of a high-velocity [up to 50 times the capillary velocity, $u_c = (\sigma_s / (\rho_l R_0))^{1/2}$] Worthington jet. Depending on the conditions, this jet may break up via a Rayleigh-Plateau instability to release one, or multiple, liquid drops into the atmosphere.

The fundamental dynamics governing the formation of jet drops from bursting bubbles are well established in scenarios devoid of any contaminant material, with significant understanding extending from very low Bond numbers [$\mathrm{Bo} \sim O(10^{-3})$] to higher Bond numbers up to $\mathrm{Bo} \approx 1$. Among many notable contributions to the field, outlined in a recent review [7], the interrelation between the nature of the capillary waves and the ejection of the Worthington jet is now well understood as a result of the works of Refs. [8,10] and collaborators. The theoretical models proposed in these references suggest that the Worthington jet forms due to the system's selection of a dominant capillary wave with wavelength λ^* during thin-film retraction. This wavelength, which scales with Oh as $\lambda^* \sim \mathrm{Oh}^{1/2}$, corresponds to that of the smallest wavelength not fully attenuated by

viscous effects. These studies have also uncovered the constant behavior of the angular velocity of the dominant capillary wave, $|u_{\theta,\mathrm{lin}}| \approx 5u_c$, as it propagates across the bubble. This angular velocity has also been demonstrated to be unaffected by Oh up to Bo ≈ 0.7 [10].

Through extensive experiments and numerical simulations, Refs. [1,4,8,11–15] (and references cited therein) have contributed to characterizing the size and velocity of the first ejected drop and the Worthington jet. Particularly noteworthy is the work of Ref. [8], which proposes relationships between Oh and the jet's velocity, u_{jet}. These relationships include $u_{\mathrm{jet}} \sim \mathrm{Oh}^{1/2}$ (Oh $\ll$ Oh$_*$), $u_{\mathrm{jet}} \sim (1 - (\mathrm{Oh}/\mathrm{Oh}_*)^{1/2})^{-1/2}$ (Oh $\approx$ Oh$_*$), and $u_{\mathrm{jet}} \sim \mathrm{Oh}^{-1}$ (Oh $>$ Oh$_*$), where Oh$_* \approx 0.043$ denotes the Oh value above which viscous effects preclude the jet from breaking. References [13] and [4] have proposed scaling laws of the form $\sim \mathrm{Oh}^{1/2}(\mathrm{Oh}_* - \mathrm{Oh})^{-3/4}$ to relate the velocity of the first ejected drop or the jet before breakup, u_{d1}, with Oh, with the latter reference also proposing an expression to include the effects of Bo. In terms of first ejected drop size, R_{d1}, numerous experimental and numerical works have confirmed the scaling derived in Ref. [13], in which R_{d1} scales with Oh as $\sim[(\mathrm{Oh}_* - \mathrm{Oh})\mathrm{Oh}^{-2}]^{5/4}$. The structurally complex interfacial phenomena that arise from surface-active material have been the subject of a handful of recent investigations. The experimental and numerical work of Refs. [16–20] for Bo $\to 0$ have reported dramatic modifications to all steps leading to jet breakup, revealing intricate relationships between the system's outcomes and surfactant properties due to the comparable nature of surfactant-related timescales and those of bubble bursting. The most notable of these modifications involves a consistent temporal retardation of bubble collapse with the addition of insoluble surfactant [sodium dodecyl sulfate (SDS)]. This retardation increases in prominence as the surfactant concentration increases but remains below the critical micelle concentration (CMC) [19]. Simulations in Ref. [16] have provided initial insights into the complex role of Marangoni stresses and reduced surface tension on the retardation dynamics. This study reported the development of a toroidal capillary wave carrying a large surfactant concentration across the bubble's domain, leading to a low surface tension bubble collapse (larger local Oh) and a fast jet ejection ($u_{\mathrm{jet}} \sim \mathrm{Oh}^{1/2}$ [8]) that is subsequently delayed by the action of Marangoni stresses. Other surfactant-induced effects unveiled in the literature relate to a reduction in the number and size of ejected drops below the CMC [19,20]. The recent experiments and theoretical framework presented in Ref. [17] expose the marked influence of surface viscoelasticity and its unequivocal departure from Newtonian surface behavior in surfactant-laden flows. This study introduces a new bursting regime featuring secondary daughter bubble entrapment during collapse and jetting suppression, which uniquely originate from the action of dilatational elastic stresses rather than Marangoni stresses. A similar jetting suppression phenomenon has been observed in bursting bubble systems in non-Newtonian liquid media and surfactant-free interfaces [21].

Despite recent strides in untangling the rich interfacial phenomena that unfold in the presence of surface-active contaminants, a few critical aspects remain elusive. While experimental observations have detected a delay in capillary wave motion, enabling estimations of capillary wave velocity in surfactant-laden systems, temporal information on the evolution of the angular position of the dominant capillary wave, θ, akin to the insights provided by Ref. [8] for clean interfaces, has not been reported before. As demonstrated throughout this paper, uncovering the dependence of θ on t is paramount to understanding the system's dynamics, representing the inherent nonlinearity and complexity of surfactant flows that are heavily influenced by surfactant parameters. Additionally, and as stated in Refs. [19,20], the exact mechanism by which the motion retardation comes about, as well as the unique influence of Marangoni stresses, is still unclear and challenging to access experimentally. The present paper builds upon previous work and presents a numerical exploration of the problem of bursting bubbles in surfactant-laden flows of varying solubility and surfactant strength, operating under non-negligible gravitational conditions (Bo $= 0.1$–5). A mechanistic rationalization of the specific role of Marangoni stresses in wave motion delay has been proposed in surfactant-laden bursting bubbles. This paper also illustrates the effects of nonvanishing Bo on capillary waves for values (Bo > 0.7) not previously reported in the literature, and how gravitational and surfactant effects converge to fully suppress jetting.

The rest of this paper is organized as follows. Section II introduces the system considered, our numerical approach, and related dimensionless parameters. Section III presents our results and discussion, focusing first on surfactant-free interfaces at large Bo, and then inspecting the striking influence of surfactants. Concluding remarks are provided in Sec. IV.

II. FORMULATION AND PROBLEM STATEMENT

A. Governing equations and dimensionless numbers

We conduct two-phase direct numerical simulations to investigate the dynamics of an isolated bursting bubble event immersed in a three-dimensional (3D) Cartesian domain denoted by $\mathbf{x} = (x, y, z)$ [refer to Fig. 1(a)]. The simulations incorporate surface-active material, and the equations presented in this paper are formulated within the framework of a hybrid font-tracking–level-set technique known as the level contour reconstruction method (LCRM). This method is employed to handle surface tension forces, the interface, and their coupling with surfactant transport. Details of this approach can be found in Refs. [22–24]. All variables and physical parameters involved in the system are rendered dimensionless via the scalings expressed by Eqs. (1), which are consistent with previous work on bursting bubbles [8,16]:

$$\tilde{\mathbf{x}} = \frac{\mathbf{x}}{R_0}, \quad \tilde{t} = \frac{t}{t_c}, \quad \tilde{\mathbf{u}} = \frac{\mathbf{u}}{u_c}, \quad \tilde{p} = \frac{p}{\rho u_c^2}, \quad \tilde{\mu} = \frac{\mu}{\mu_l},$$

$$\tilde{\rho} = \frac{\rho}{\rho_l}, \quad \tilde{\sigma} = \frac{\sigma}{\sigma_s}, \quad \tilde{\Gamma} = \frac{\Gamma}{\Gamma_\infty}, \quad \tilde{C} = \frac{C}{C_\infty}, \quad \tilde{C} = \frac{C_s}{C_\infty}, \tag{1}$$

where $\tilde{t}$, $\tilde{\mathbf{u}}$, $\tilde{p}$, $\tilde{\mu}$, $\tilde{\rho}$, and $\tilde{\sigma}$ represent time, velocity vector, pressure, local viscosity, density, and surface tension, respectively; $\tilde{\Gamma}$, $\tilde{C}$, and $\tilde{C}_s$ are surfactant concentration at the interface, bulk, and bulk concentration at the interface, respectively. Hereinafter, tildes represent dimensionless variables, and the subscripts l and g distinguish between the liquid and gas phases. In the above equations, R_0 is the bubble size, $u_c = \sqrt{\sigma_s/(\rho_l R_0)}$ is the velocity timescale, $t_c = R_0/u_c = \sqrt{\rho_l R_0^3/\sigma_s}$ is the capillary timescale, and σ_s is the surface tension in a surfactant-free interface. Surfactant-related variables are scaled on the saturation interface surfactant concentration or maximum packing, Γ_∞, and the initial bulk surfactant concentration, C_∞. In what follows, we refer to all variables by their name to refer to their dimensionless version, unless stated otherwise.

The equations governing the simulation, presented herein, are expressed in dimensionless form under the assumptions of Newtonian fluids, immiscible phases, and incompressible flow. The continuity and momentum equations, written within a one-fluid formulation, are provided in Eqs. (2)–(4):

$$\nabla \cdot \tilde{\mathbf{u}} = 0, \tag{2}$$

$$\tilde{\rho}\left(\frac{\partial \tilde{\mathbf{u}}}{\partial \tilde{t}} + \tilde{\mathbf{u}} \cdot \nabla \tilde{\mathbf{u}}\right) + \nabla \tilde{p} = -\text{Bo}\,\mathbf{i}_z + \text{Oh}\,\nabla \cdot [\tilde{\mu}(\nabla \tilde{\mathbf{u}} + \nabla \tilde{\mathbf{u}}^T)] + \int_{\tilde{A}(\tilde{t})} (\tilde{\sigma}\tilde{\kappa}\mathbf{n} + \nabla_s \tilde{\sigma})\delta(\tilde{\mathbf{x}} - \tilde{\mathbf{x}}_f)d\tilde{A}, \tag{3}$$

$$\tilde{\rho}(\mathbf{x}, t) = \rho_g/\rho_l + (1 - \rho_g/\rho_l)\mathcal{H}(\tilde{\mathbf{x}}, \tilde{t}),$$

$$\tilde{\mu}(\mathbf{x}, t) = \mu_g/\mu_l + (1 - \mu_g/\mu_l)\mathcal{H}(\tilde{\mathbf{x}}, \tilde{t}), \tag{4}$$

where $\mathcal{H}$ is a smoothed Heaviside function that adopts the value of zero in the gas phase and unity in the liquid phase. This function is computed directly from the interface and solved numerically with a smooth transition across three or four cells [22,23]. As introduced in Sec. I, Bo denotes the Bond number, and Oh is the Ohnesorge number [see Eqs. (9) for their definitions]. In Eq. (3), the last two terms on the right-hand side (RHS) account for the normal and tangential components of the surface tension forces, $\tilde{\mathbf{F}}_\sigma$. The normal component arises from the average localized surface tension, while the tangential component, or Marangoni stresses, acts on the interface due to surfactant-induced surface tension variations across the interface. In the definitions, $\tilde{\kappa}$ is twice the mean interface

curvature, $\mathbf{n}$ represents a unit vector normal to the interface pointing towards the liquid phase, $\tilde{A}(\tilde{t})$ denotes the time-dependent interface area, and $\delta(\tilde{\mathbf{x}} - \tilde{\mathbf{x}}_f)$ is a Dirac delta function. This δ function vanishes everywhere except for the interface (located at $\tilde{\mathbf{x}} = \tilde{\mathbf{x}}_f$); $\boldsymbol{\nabla}_s = (I - \mathbf{nn}) \cdot \boldsymbol{\nabla}$ signifies the surface gradient operator.

Surfactant transport is resolved in both the liquid bulk phase and at the interface via the nonpassive convection-diffusion expressions of Eqs. (5) and (6), according to the well-established formulation by Refs. [25,26] (and references therein):

$$\frac{\partial \tilde{\Gamma}}{\partial \tilde{t}} + \boldsymbol{\nabla}_s \cdot (\tilde{\Gamma}\tilde{\mathbf{u}}_t) = \frac{1}{\mathrm{Pe}_s}\nabla_s^2\tilde{\Gamma} + \mathrm{Bi}(k\tilde{C}_s(1 - \tilde{\Gamma}) - \tilde{\Gamma}), \tag{5}$$

$$\frac{\partial \tilde{C}}{\partial \tilde{t}} + \tilde{\mathbf{u}} \cdot \boldsymbol{\nabla}\tilde{C} = \frac{1}{\mathrm{Pe}_c}\nabla^2\tilde{C}, \tag{6}$$

$$\mathbf{n} \cdot \boldsymbol{\nabla}\tilde{C}|_{\mathrm{interface}} = -\mathrm{Pe}_c\mathrm{Da}\mathrm{Bi}(k\tilde{C}_s(1 - \tilde{\Gamma}) - \tilde{\Gamma}), \tag{7}$$

where $\tilde{\mathbf{u}}_t = (\tilde{\mathbf{u}}_s \cdot \mathbf{t})\mathbf{t}$ is the tangential projection of the surface velocity vector, $\tilde{\mathbf{u}}_s$. Within this formulation, surfactant is exchanged between the interface and the bulk region immediately adjacent via the source term written in Eq. (7). The dependence of surface tension on variations in $\tilde{\Gamma}$ is computed via the nonlinear Langmuir equation of state, which assumes that noninteracting surfactant molecules occupy finite-sized sites on a lattice [27]. This expression reads

$$\tilde{\sigma} = \max(\epsilon_\sigma, 1 + \beta_s \ln(1 - \tilde{\Gamma})), \tag{8}$$

with $\beta_s = \mathcal{R}T\Gamma_\infty/\sigma_s$ representing surfactant elasticity or surfactant "strength," as defined in previous investigations [26,28,29], and $\epsilon_\sigma = 0.05$. Here, $\mathcal{R}$ is the ideal gas constant and T the system's absolute temperature. The ϵ_σ parameter corresponds to a limit placed on $\tilde{\sigma}$ and introduced in the formulation to circumvent the issue of unphysical negative surface tensions predicted by the Langmuir expression in nondilute systems where surfactant concentration approaches the maximum packing ($\tilde{\Gamma} \rightarrow 1$) [24,26]. The dimensionless groups that govern the system are defined here as

$$\mathrm{Bo} = \frac{\rho_l g R_0^2}{\sigma_s}, \quad \mathrm{La} = \mathrm{Oh}^{-2} = \frac{\rho_l \sigma_s R_0}{\mu_l^2}, \quad \mathrm{Bi} = \frac{k_d R_0}{u_c}, \quad k = \frac{k_a C_\infty}{k_d}, \quad \mathrm{Da} = \frac{\Gamma_\infty}{R_0 C_\infty}, \quad \mathrm{Pe}_{s,c} = \frac{u_c R_0}{D_{s,c}}, \tag{9}$$

where Bo characterizes the interplay between gravitational and capillary forces, while La quantifies the relative significance of viscous to capillary forces; the Biot number, Bi, serves as a metric for surfactant solubility, comparing the capillary and desorptive, $t_d = k_d^{-1}$, timescales. The parameter k directly influences the balance between surfactant adsorption, $t_{ad} = (k_a C_\infty)^{-1}$, and desorption timescales. The Damköhler number, Da, provides insight into the initial surfactant saturation, while $\mathrm{Pe}_{s,c}$ denotes the Péclet numbers associated with the significance of surfactant diffusive effects on both the interface (modulated by diffusivity D_s) and the liquid bulk (modulated by diffusivity D_c) with respect to the characteristic timescale of the system, t_c.

In the present study, we compute the dimensionless Marangoni stresses, $\tilde{\tau}_m$, by using Eq. (10)

$$\tilde{\tau}_m \equiv \boldsymbol{\nabla}_s\tilde{\sigma} \cdot \mathbf{t} = -\frac{\beta_s}{1 - \tilde{\Gamma}}\boldsymbol{\nabla}_s\tilde{\Gamma} \cdot \mathbf{t}. \tag{10}$$

The variation of $\tilde{\tau}_m$ with respect to β_s positions surfactant strength as a regulator of Marangoni stress magnitude. In our convention, positive values of Marangoni stresses are observed in regions transitioning from higher to lower $\tilde{\Gamma}$.

In addition to modulating surface pressure [$\Pi = -\beta_s\sigma_s\ln(1 - \frac{\Gamma}{\Gamma_\infty})$; see Eq. (8)] and Marangoni stresses, β_s acts as a direct regulator of various thermodynamic concepts within the Langmuir isotherm framework, including the Gibbs-Marangoni moduli and the Marangoni number, represented here as Ma. The standard expression for the Marangoni modulus, E_0, for the Langmuir isotherm can be rearranged in terms of β_s as $E_0 \equiv \Gamma\frac{\partial \Pi}{\partial \Gamma}|_N = \frac{\beta_s\sigma_s\Gamma}{\Gamma_\infty(1-\Gamma/\Gamma_\infty)}$ (with N being the number

of moles), underscoring the direct influence of β_s on this parameter [27]. For identical values of Γ, higher β_s values result in greater resistance to interfacial compression, leading to increased interfacial "rigidification" or "immobilization." E_0 can also be interpreted as the work done by the process of "squeezing" surfactant molecules together [27].

Based on the well-known definition of Ma as the ratio between characteristic Marangoni and viscous stresses ($\tau_{m,ch}$ and $\tau_{\mathrm{vis},ch}$, respectively [27,28]), and using the initial surfactant concentration, Γ_0, as a characteristic state, Eq. (11) provides a definition of Ma for the present system:

$$\mathrm{Ma} = \frac{\tau_{m,ch}}{\tau_{\mathrm{vis},ch}} = \frac{\beta_s \sigma_s}{\mu_l u_c}. \tag{11}$$

As demonstrated by the above equation, larger β_s values directly lead to higher Ma, indicating an increased significance of Marangoni stresses relative to viscous stresses.

B. Numerical method

For our calculations, we employ the code BLUE, which is based on the LCRM. This method and code have been successful in reproducing both experimental and numerical data in a plethora of applications involving complex interfacial flow instabilities with contaminants, including drop coalescence [30], ligament breakup [31], turbulent jets [32], microfluidics [33], falling film [34], elongated bubbles [35,36], and, indeed, bursting bubbles for very small Bond number [16]. We present in this section a brief summary of the most relevant aspects of our method and refer the reader to Refs. [22–24] for further details. The field equations presented above are resolved by utilizing a finite-difference method with a fixed Eulerian grid. Spatial derivatives of the Eulerian grid fields are discretized through a standard cell-centered scheme for most terms, except for the nonlinear convective terms, which employ a second-order essentially nonoscillatory (ENO) procedure [37] on a staggered grid. The viscous term in the momentum equation is discretized using a second-order centered difference scheme. Temporal terms are handled with a second-order gear method [38], incorporating implicit time integration for the viscous terms.

The interface is tracked with a front-tracking method and reconstructed using a level-set approach [22,39]. The connection between Lagrangian and Eulerian grid is achieved through Peskin's [40] well-known immersed boundary method. The front-tracking method utilizes a deformable grid with Lagrangian elements discretized using a triangular mesh. These Lagrangian elements are advected by integrating equation $d\mathbf{x}_f/dt = \mathbf{V}_f$, where $\mathbf{V}_f$ represents the interface fluid velocity, which displaces the vertices of the Lagrangian triangular mesh, $\mathbf{x}_f$. This integration is performed using a second-order Runge-Kutta method.

C. Simulation setup and timescales

The computational domain for most simulations consists of a rectangular box of size $12R_0 \times 12R_0 \times 6R_0$, where the latter dimension corresponds to the domain's height [see Fig. 1(a)]. We highlight that this height is smaller than that of previous numerical studies, such as the $15R_0$ used in Ref. [16] or the $8R_0$ used in Ref. [21] as our focus is specifically on the large Bond number (Bo = 0.5–5) regime. In this regime, the system exhibits a significant reduction in the velocity and length of the jet [4,41]. During testing, we found this domain size to be appropriate to render radially and height-related boundary effects negligible. For the simulations characterized by Bo = 0.1, the domain size was increased to $(12R_0)^3$.

The system is initiated with a static equilibrated bubble positioned beneath the liquid-gas interface, shaped according to the Young-Laplace equation. This equation dictates the bubble's morphology based on a static quasiequilibrium between surface tension and gravity, directly influenced by the choice of Bo [5,42]. A cross section of the initial bubble shapes for the four tested Bo values is depicted in Fig. 1(b). Notice that, as Bo increases, there is a clear departure from sphericity, accompanied by reduced immersion in the liquid bulk. In adherence to the common approach in numerical investigations of bursting bubbles, even at Bo > 1 [15], the simulations commence at the point when the liquid cap completes its draining process. This simplification, enabling the exclusion

of the liquid cap, is justified by the markedly larger Taylor-Culick velocity associated with cap retraction time, u_{TC}, in comparison to the system's main phenomena. Under our conditions, u_{TC} is larger than our characteristic velocity scale u_c by three to two orders of magnitude. We nonetheless discuss the implications of neglecting the cap dynamics at large Bo and the caveats of our results at the end of Sec. III A and Appendix C.

We employ a structured uniform grid of resolution $(768)^2 \times 384$ [$(768)^3$ for Bo $= 0.1$], ensuring converged and mesh-independent results during testing for both the present study and our prior work on bursting bubbles [16]. This grid resolution proves crucial, particularly at the instants of jet ejection and breakup, where large velocities are involved. For a comprehensive validation of our code, extending beyond our prior work on bursting bubbles [16], please refer to Appendix A. We seek solutions to the governing equations subject to Neumann boundary conditions for the lateral and bottom boundaries in all variables, except for pressure, for which no-slip conditions are utilized. Surfactant material is initialized with an equilibrium condition between the bulk and interface. By equating the last term on the RHS of Eq. (5) to zero and considering $\tilde{C} = 1 = \tilde{C}_s$, the initial interface surfactant concentration is set to $\tilde{\Gamma}(\mathbf{x}, t = 0) = \tilde{\Gamma}_0 = k/(k+1) = 0.55$. This concentration is kept constant in all simulations to isolate the "pure" effects of other, less understood surfactant parameters, such as solubility and surface elasticity. This approach also allows for a clearer analysis of the relationship between these parameters and Marangoni stresses.

We examine the impact of surfactant solubility within the range Bi $= 0$–10 and surfactant strength within the range $\beta_s = 0.05$–1, equivalent to Ma $= 15$–311, which is in line with previously reported Ma for common surfactants (Ma $\sim O(10^1)$ [43]). As implied in Eqs. (9), our formulation specifies that Bi $= 0$ denotes an insoluble surfactant (i.e., no surfactant desorption), while the limit Bi $\to \infty$ corresponds to a surfactant-free interface. The additional dimensionless parameters associated with surfactant remain constant at $k = 1.22$, Pe$_{s,c} = 100$, and Da $= 1$. Along with the above parameters, we vary both Bo and La in the ranges $0.1 < $ Bo < 5 and $10^4 < $ La $< 10^6$ ($10^{-2} > $ Oh $> 10^{-3}$). These La conditions are well above the "optimal" value of La ≈ 1000, where the system approaches a singularity at the instant of collapse and the maximum (minimum) jet velocity (drop size) is attained for Bo $\to 0$ [8,41].

Our selection of dimensionless parameter values is informed by the characteristics of commonly employed commercial surfactants in bursting bubble applications, such as SDS and Triton X-100 (TX100) [19,20]. These surfactants exhibit diffusivities in the range of $D_{s,c} = O(10^{-10}$–$10^{-9})$ m^2 s^{-1}, resulting in corresponding Péclet numbers of Pe$_{s,c} = O(10^3$–$10^6)$. This indicates that surfactant transport and rearrangement events across the interface are unlikely to be dominated by interfacial surfactant diffusion. Our chosen conditions also ensure the significant involvement of Marangoni stresses in our system, given the comparable nature of the Marangoni timescale, $t_m = \mu_l R_0/(\Delta\sigma) = O(10^{-2})$ s, with those associated with sorption kinetics, $O(10^{-2})$–$O(10^{-1})$ s [44]. Furthermore, we operate at sufficiently low bulk surfactant concentrations to neglect the micelle formation and its potential effects on the system.

III. RESULTS AND DISCUSSION

A. Uncontaminated interfaces: Buoyancy effects on capillary wave velocity and Worthington jet

Let us begin our discussion by analyzing the influence of gravitational effects in surfactant-free interfaces. Figure 2 offers a qualitative comparison of the system's behavior before [Figs. 2(a)–2(d)] and after [Figs. 2(e)–2(h)] bubble collapse for Bo $= 0.5$ and Bo $= 5$ in a representative case at Oh $= 3.21 \times 10^{-3}$. In order to make temporal one-to-one comparisons between different cases and bursting stages, we define a comparative time, $T = (\tilde{t} - \tilde{t}_0)/\tilde{t}_0$, which takes the bubble collapse time, t_0, as a reference and compares the system's dynamics at the same temporal distance from collapse. Thus, $T < 0$ ($T > 0$) designates the precollapse (postcollapse, or jetting) stages. The pressure fields depicted in the figures are presented in relation to the pressure at the pool-atmosphere interface. As detailed in Sec. I, the process of liquid cap retraction concludes in the outset of capillary wave motion away from and down the cavity. The latter set of waves ultimately converges at the bubble's
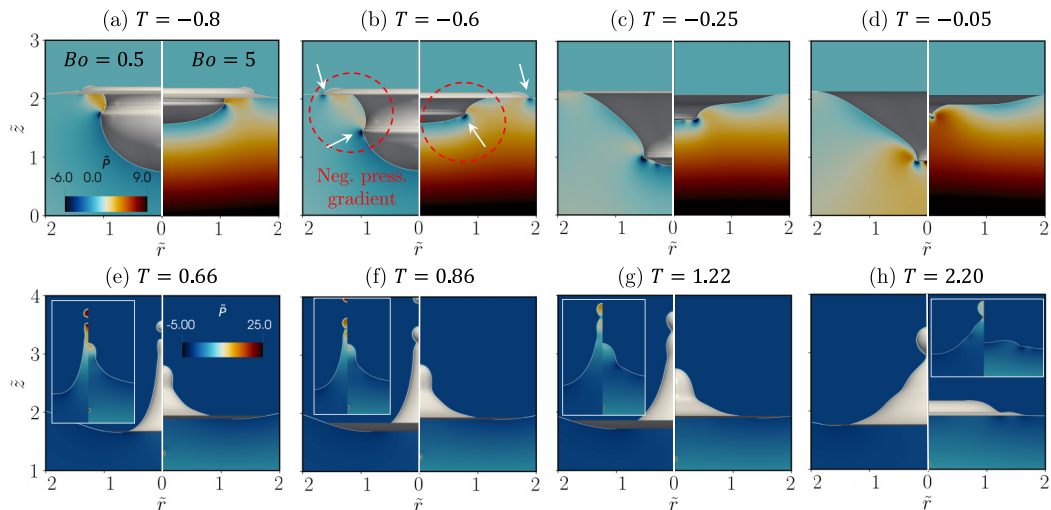
FIG. 2. Bubble bursting dynamics in surfactant-free interfaces: comparison of pressure fields and interface shape at the same T for a moderate $Bo = 0.5$ on the left half and a large $Bo = 5$ on the right half. (a)–(d) Precollapse dynamics; (e)–(h) Worthington jet motion and drop detachment. The insets in (e)–(h) focus on the emerging jet's pressure fields, the white arrows point to the location of the dominant capillary wave, and the dashed red circles highlight the negative pressure gradients. For all cases in this figure, $\mathrm{Oh} = 3.21 \times 10^{-3}$ $(\mathrm{La} = 9.7 \times 10^{4})$.

bottom, giving rise to the Worthington jet. The dominant capillary waves (i.e., those characterized by the largest curvature [8]) are clearly seen at the low-pressure locations marked by white arrows.

During the early and middle bursting stages ($T < -0.25$), the high-pressure regions immediately upstream of the bubble's dominant wave create a negative pressure gradient, directing the flow downward in the z direction and facilitating capillary wave motion towards the bottom of the cavity, as depicted in red in the figure. In the case of $Bo = 5$, this negative pressure gradient competes with the upward pressure gradient between the high-pressure liquid bulk and the low-pressure region beneath the bubble's bottom. The discussion of subsequent figures will elucidate how this competition between pressure gradients is accountable for delaying capillary wave motion, resulting in a lower average motion velocity above $Bo = 1$. Furthermore, we will explore how these retarding gravitational effects do not impact the linearity of the motion, in contrast to the effects induced by surfactant.

The postcollapse phenomena of Figs. 2(e)–2(h) underscore the anticipated stabilizing influence of gravity on capillary breakup and jet growth, resulting in complete avoidance of pinch-off and notably smaller jets for $Bo = 5$ across all tested La values (refer to Appendix A for a compilation of the effects of La and Bo on jet length and velocity at the instant before the first pinch-off, as well as the size of the first ejected drop). As is evident from the interfacial shapes in Fig. 2, the deceleration of the jet due to gravitational forces continues to shape the jet's dynamics following the initial pinch-off event for $Bo = 0.5$. Notably, we observe that the maximum dimensionless jet length achieved, irrespective of pinch-off occurrences, exhibits a relationship with Bo given approximately by $(L_{\mathrm{jet}}/l_{\mathrm{vis}})_{\mathrm{Max}} \sim \mathrm{Bo}^{-0.36}$ across all three considered La values, in contrast to the moment of the first pinch-off where $(L_{\mathrm{jet}}/l_{\mathrm{vis}}) \sim \mathrm{Bo}^{-0.16}$. Here, l_{vis} denotes the viscous length scale, defined in Eq. (A1). This inverse relationship between jet length and Bo is in agreement with the observations of Ref. [15]. We highlight that the threshold for jet drop production in our simulations also aligns completely with the Oh-Bo maps indicating production or no production from the same reference (see Fig. 4 in that reference).
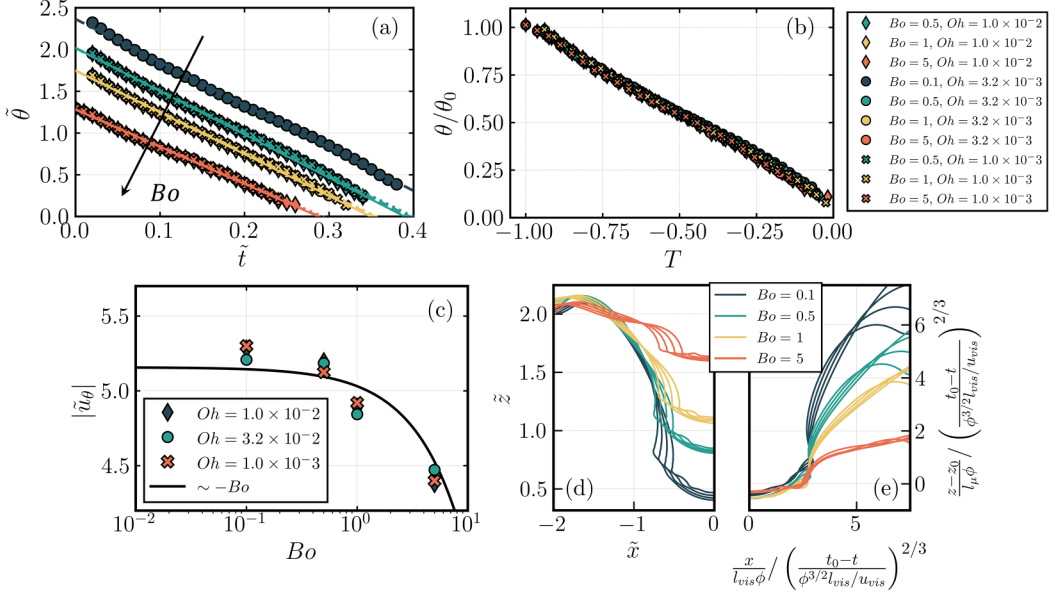
FIG. 3. Dynamics of capillary wave velocity and interfacial shape in surfactant-free interfaces: effect of Bo and Oh. (a) Temporal evolution of $\tilde{\theta}$. The markers represent our simulation data (taken every $\Delta\tilde{t} = 0.01$) and the line corresponds to a linear fit of the data; (b) data scaled by θ_0 and $\tilde{t}_0$, showcasing the constant nature of the capillary wave velocity, even at the largest Bo tested, Bo = 5; (c) compilation of $|\tilde{u}_\theta|$ vs Bo data, wherein -0.126Bo with $R^2_{\text{pow}} = 0.9833$; (d) and (e) interfacial shapes for varying Bo across four different times in the range $t_0 - t \approx 6t_{\text{pre}} - 10t_{\text{pre}}$ in the standard Cartesian space and in the rescaled spaced proposed in [14]; z_0 represents the point in the vertical coordinate where jet ejection occurred. For these cases, Oh = 3.21×10^{-3}.

In Fig. 3, we plot our measurements of angular location of the dominant (or "strongest," as referred to in other works [21]) capillary wave, $\tilde{\theta}$, as it transverses down the bubble's domain. This dominant wave corresponds to the sharpest (of lowest wavelength) wave not fully dampened by viscous dissipation [8,9]. Our $\tilde{\theta}$ numerical observations align with the methodology outlined by Gordillo and Rodríguez-Rodríguez [8], where the angle for each Bo is measured from the bubble's initial center point, as illustrated in Figs. 1(b) and 1(c). In Fig. 3(a), we observe a nearly complete marker superposition in the $\tilde{\theta}$ vs $\tilde{t}$ data for all Oh tested under the same Bo. This alignment not only reaffirms prior findings indicating a negligible influence of Oh on capillary wave velocity up to Bo = 0.7, as demonstrated by previous researchers (see supplementary information in Ref. [10]), but also extends this observation to higher Bond numbers (Bo < 5). It is essential to note that the downward shift of the data for increasing Bo values is attributed to variations in the initial angle, $\tilde{\theta}_0$, which itself results from differences in the initial submersion degrees of the bubbles for different Bo.

It is also noteworthy that, akin to prior studies utilizing other numerical methods, the emergence of high velocities and pressures as collapse is approached impedes the unambiguous tracking of $\tilde{\theta}$ as $\tilde{t} \to \tilde{t}_0$. Consequently, our measurements do not precisely terminate at $\tilde{\theta} = 0$. The calculated slope values from our available data (normalized by u_c), denoted as $\tilde{u}_\theta = u_c^{-1}(\theta_f - \theta_0)/t_f$, are compiled in Fig. 3(c). Inspection of these values reveals a transition from $|u_\theta| \approx 5$ (fully consistent with Refs. [8,10]) at Bo = 0.1, 0.5, 1 to $|\tilde{u}_\theta| \approx 4.35$ at Bo = 5. Although small, this velocity decrease is found to persist for all Oh tested, suggesting an approximate relation of the form $|\tilde{u}_\theta| \sim -$Bo, as seen by the curve displayed in the figure for reference. Figure 3(b), along with the R^2 values of a linear fit (ranging from 0.998 to 0.999 in all cases), clearly illustrate the constant nature of the capillary wave velocity in surfactant-free interfaces, even at large Bo. The linearity of $\tilde{\theta}$ vs $\tilde{t}$ enables

the collapse of all data points using the comparative time, $T = (\tilde{t} - \tilde{t}_0)/\tilde{t}_0$, and the initial location of the capillary wave.

This $\tilde{\theta}$ collapse can be related to the well-known interfacial shape self-similar behavior featured in uncontaminated interfaces. This self-similarity has been shown to underpin the dynamics of collapsing structures that lead to jetting, such as bursting bubbles and interfacial waves [12,14,45,46]. An inviscid and incompressible balance of inertia and capillarity in scenarios neglecting gravity leads to an interface shape scaling that obeys $h(r, t) \sim |t_0 - t|^{2/3}$. The work of Ref. [14] has demonstrated that this scaling is valid before and after bubble collapse in a specific range of temporal distances from collapse. During the precollapse period, this range corresponds to $t_0 - t \approx 6t_{\text{pre}} - 10t_{\text{pre}}$, where $t_{\text{pre}} = \phi^{3/2} l_{\text{vis}}/u_{\text{vis}}$ is the characteristic time of the capillary wave; ϕ, l_{vis}, and u_{vis} are defined in Eq. (A1). As $t_0 - t \to 0$ and the curvature inversion that leads to the nascent jet takes place, this self-similarity is disrupted.

Based on the above, we plot in Figs. 3(d) and 3(e) our computed interfacial shapes for different Bo and for Oh $= 3.21 \times 10^{-3}$ (La $= 97\,000$) in the standard Cartesian space and in the rescaled space proposed in Ref. [14]. Lines of the same color correspond to the same Bo at four different times falling approximately within the $t_0 - t \approx 6t_{\text{pre}} - 10t_{\text{pre}}$ window. We observe reasonable interfacial collapse in the region surrounding the bottom of the cavity, both across varying times for individual cases and between different Bo values. Although reasonable, the fact that the rescaled profiles do not exactly fall within a single universal line is a testament of the non-negligible gravitational effects present at large Bo. We also draw attention to the fact that this scaling was originally reported to be valid only for La ≈ 1000–5000 during precollapse, further explaining the incomplete collapse of the curves. An additional examination of the effect of gravity on the capillary waves and jet growth or breakup in terms of kinetic, surface, and viscous dissipation energy can be found in Appendix B.

Before transitioning into the effects of surfactants, it is imperative to discuss a few implications of our computational setup. Specifically, we must address the ramifications of neglecting the dynamics of the retracting liquid cap at large Bo. While this approach is common in computational studies, even up to Bo ≈ 5 [15], several experimental works have hinted at the emergence of markedly different jets as Bo increases (see, for instance, Fig. 1 in Ref. [15] or Fig. 6 in Ref. [20]). As dictated by the Young-Laplace expression, instances characterized by larger Bo entail reduced submersion of the bubble into the liquid pool, leading to a liquid film with much greater surface area exposed to the atmosphere. Consequently, the likelihood of the first cap hole appearing precisely at the flow origin (i.e., at $\tilde{r} = 0$ or $\tilde{x} = 6$ in radial and Cartesian coordinates, respectively), from which fully symmetric cap retraction, capillary wave motion, and jet ejection phenomena unfold, is greatly diminished. The appearance of a liquid cap hole shifted from the axis center triggers an imbalanced capillary wave motion and a wave convergence point shifted away from $\tilde{x} = 6$, which, in turn, leads to the ejection of nonsymmetrical jets. A schematic illustrating this mechanism can be found in Appendix C (Fig. 14). The nucleated hole at $\tilde{x} > 6$ elicits a temporal delay in the dynamics at $\tilde{x} < 6$, approximated by the cap retraction time, $t_{TC} \sim E/u_{TC} = (R_0^3/l_c^{3/2})((\rho_l)/(2\sigma_s\omega))^{1/2}$, where $E \sim R_0^2/l_c$ represents the liquid cap's extent, $l_c = \sqrt{2\sigma_s/(\rho_l g)}$ is the capillary length scale, and $\omega = 10^3$ [6,7]. Thus, capillary waves traveling at the $\tilde{x} > 6$ side at a velocity equal to approximately $4u_c$ to $5u_c$ meet their counterparts not at $\tilde{x} = 6$, but at $\tilde{x} < 6$, leading to complex wave interactions and nonsymmetric jet formation. As this retardation time increases with gravity and R_0, one can envision a scenario where it becomes comparable to the characteristic time of the problem, t_c. A comprehensive investigation into this phenomenon of nonsymmetric jets and unbalanced capillary wave motion is deferred to future studies.

B. Contaminated interfaces: Phenomenology of bubble collapse

1. Surfactant-induced wave retardation and break of linearity

We now direct our focus towards the intriguing and notably distinct dynamics that emerge with the introduction of surface-active contaminants into the system. In Fig. 4, we present a qualitative
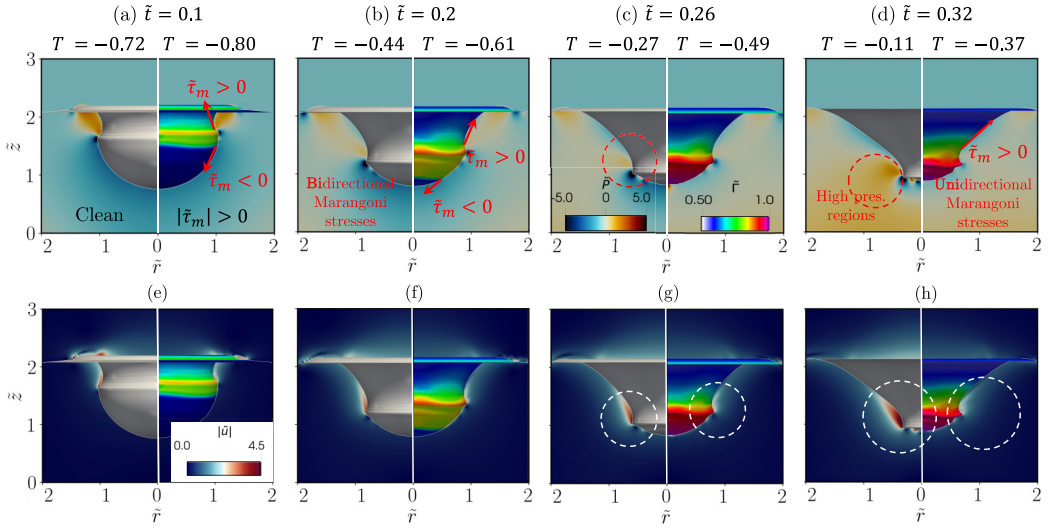
FIG. 4. Surfactant-driven capillary wave motion delay: comparison of temporal evolution (at the same $\tilde{t}$) of precollapse bubble for surfactant-free interfaces on the left half and insoluble surfactant (Bi$=0$, $\beta_s=0.3$, Ma$=93.43$) on the right half. For reference, the corresponding values of T are reported for each case; (a)–(d) pressure fields; (e)–(h) velocity magnitude fields. The red arrows schematically indicate the primary direction of Marangoni stresses, suggesting an eventual dominance of motion-delaying positive Marangoni stresses. The red dashed circles highlight the significantly larger negative pressure gradient in clean cases [12], while the white dashed circles illustrate the stabilizing effect of surfactant on flow velocity. For all cases in this figure, Bo $= 0.5$, and Oh $= 3.21\times10^{-3}$.

comparison of wave evolution for two scenarios: a clean case (left half, denoted as "Clean") and a case with insoluble surfactant characterized by $\beta_s = 0.3$ (right half, denoted as "$|\tilde{\tau}_m| > 0$," whose interface is colored by $\tilde{\Gamma}$), Bo $= 0.5$, and Oh $= 3.21\times10^{-3}$. The values for the remaining surfactant-related dimensionless groups are set out in Sec. II C. Each column in the figure corresponds to a distinct dimensionless time, and the background contour plots depict pressure [Figs. 4(a)–4(d)] and velocity magnitude [Figs. 4(e)–4(h)].

A first inspection of Fig. 4 reveals a noticeable delay in the motion of the dominant capillary wave, whose effects are accentuated in time, as demonstrated in the upcoming discussions. This delay has been reported in a few experimental and numerical studies involving various contaminants, including surfactants [17,19,20,47]. Surfactant-driven delays in bubble collapse time range from 35% to 70%, depending on the initial surfactant concentration, aligning well with our numerical results. The similarities between the surfactant-laden and surfactant-free pressure contour plots in Fig. 4 indicate that surfactant-induced retardation does not completely prevent wave convergence and jet formation for the current parameters.

In the case of surfactants, the initially imposed homogeneity of interface surfactant concentration ($\tilde{\Gamma}_0 = 0.55$) is promptly destabilized by the substantial capillary pressure stemming from the high-curvature ($|\tilde{\kappa}| \sim O(10)$ at Oh $= 3.21\times10^{-3}$) region connecting the bubble and the liquid pool-atmosphere interface (see highlighted region in Fig. 1). As the dominant wave traverses down the bubble, propelled by the negative pressure gradient, a high-$\tilde{\Gamma}$ toroidal structure is formed in the vicinity of the dominant wave, from which Marangoni stresses arise [refer to Fig. 5(j) for the temporal evolution of $\tilde{\Gamma}$ evaluated at the location of the dominant capillary wave location, denoted as $\tilde{\Gamma}|_{\tilde{\partial}}$]. The action of these Marangoni stresses ultimately brings about a consistent reduction in capillary wave velocity, as seen next in our analysis of Fig. 5 and discussed extensively in Sec. III B 2. It also causes a generalized flow stabilization, as evidenced by the noticeably lower flow
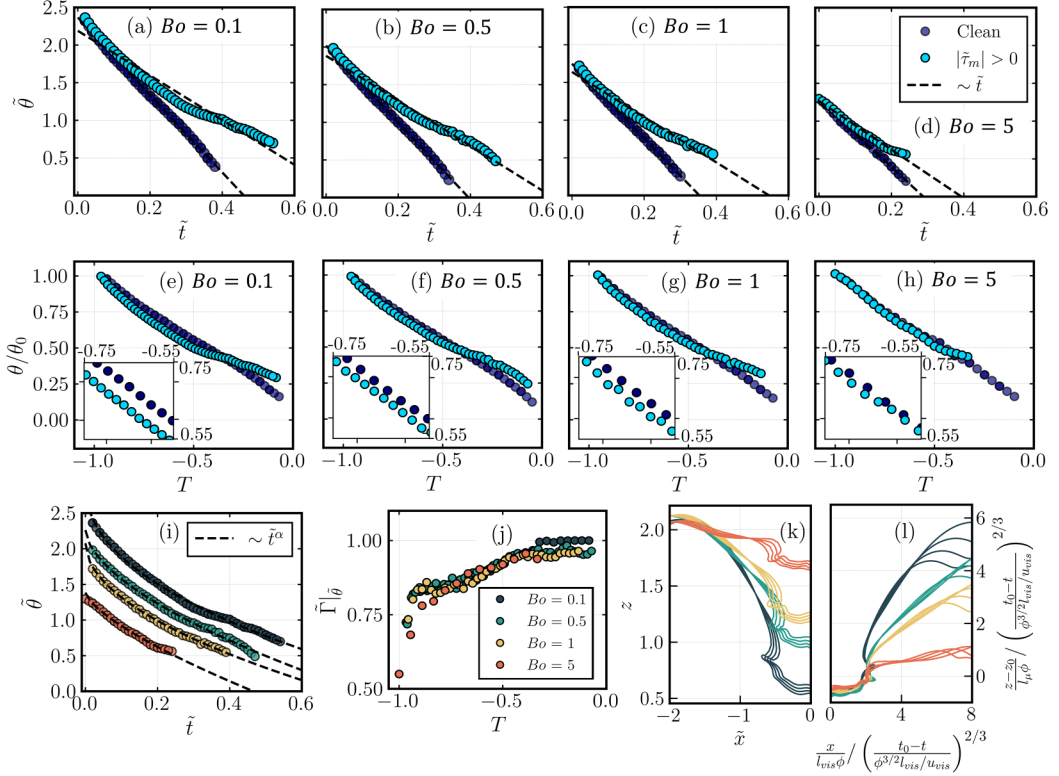
FIG. 5. Effect of insoluble surfactant (Bi = 0, $\beta_s = 0.3$, Ma = 93.43) on the dynamics of the capillary wave velocity: (a)–(d) temporal evolution of $\tilde{\theta}$; (e)–(h) data scaled by θ_0 and $\tilde{t}_0$, showcasing the break of linearity and noncollapsed solutions of contaminated interfaces vs surfactant-free interfaces; (i) direct comparison of capillary wave dynamics in surfactant-laden cases for varying Bo: the markers represent our simulation data (taken every $\Delta\tilde{t} = 0.01$), the lines correspond to linear or power-law fits of the data, and the values of the exponent α for each Bo are found in Table I; (j) interface surfactant concentration evaluated at the location of the dominant capillary wave; (k)–(l) interfacial shapes for varying Bo across four different times in the range $t_0 - t \approx 6t_{\text{pre}}$–$10t_{\text{pre}}$ in the standard Cartesian space and in the rescaled spaced proposed in Ref. [14]. z_0 represents the point in the vertical coordinate where jet ejection occurred. For all the cases in this figure, Oh = 3.21×10^{-3}.

velocities in surfactant cases shown in Figs. 4(e)–4(h) and the kinetic energy analyses of Ref. [16] [see Fig. 6(a) of this reference].

In Figs. 5(a)–5(d), we present the temporal evolution of the dominant capillary wave angular location from our insoluble surfactant simulations across varying Bo values, juxtaposed with their surfactant-free counterparts. A consistent pattern of wave retardation is observed across all Bo values, as discussed before in Fig. 4. It is worth noting that our surfactant plots show the last recoverable $\tilde{\theta}$ value before the singularity occurred in the simulations. This limitation arises due to the high pressures and velocities near and at the moment of jet ejection, complicating the accurate determination of $\tilde{\theta}$. These challenges are more pronounced in surfactant cases due to significantly larger local Oh, resulting from the high $\tilde{\Gamma}$ at the wave focusing point [$T \approx 0$; refer to Figs. 4(d), 4(h), and 5(j)].

In addition to wave retardation, Figs. 5(a)–5(d) showcase a nonlinear trend in the $\tilde{\theta}$ vs $\tilde{t}$ data (black dashed lines and corresponding R^2_{lin} values of a linear fit in Table I). Further reinforcing this nonlinearity, Fig. 5(i) and the last two columns of Table I demonstrate that $\tilde{\theta}$ evolves in close

TABLE I. Comparison of capillary wave velocity in clean interfaces and in the presence of insoluble surfactant (Bi = 0, $\beta_s = 0.3$, Ma = 93.43). R^2_{lin} represents the coefficient of determination of the linear fits shown in Figs. 5(a)–5(d) and R^2_{pow} those of the power-law fits for the surfactant cases, shown in Fig. 5(i). These fits are of the form $\tilde{\theta} \sim \tilde{t}^{\alpha}$, where α is the best-fit exponent.

Bo	Clean			$|\tilde{\tau}_m| > 0$				
	$|\tilde{u}_\theta|$	$|\tilde{u}_{\theta,\text{lin}}|$	R^2_{lin}	$|\tilde{u}_\theta|$	$|\tilde{u}_{\theta,\text{lin}}|$	R^2_{lin}	α	R^2_{pow}
0.1	5.228	5.145	0.998	3.202	2.967	0.961	0.456	0.997
0.5	5.185	5.108	0.998	3.315	2.987	0.980	0.587	0.998
1	4.844	4.951	0.999	3.125	3.003	0.975	0.517	0.998
5	4.472	4.450	0.998	3.068	3.216	0.983	0.707	0.996

agreement with a power law $\tilde{\theta} \sim \tilde{t}^{\alpha}$, where α generally increases with Bo, hinting at weakened surfactant effects with increased buoyancy. Figures 5(e)–5(h) highlight a critical feature of bursting bubbles with surfactants. The nonlinear nature of $\tilde{\theta}$ vs $\tilde{t}$ in surfactant cases prevents data collapse using T and $\tilde{\theta}_0$, unlike the clean cases for all Bo and Oh [see Fig. 3(b)]. This noncollapsing behavior between surfactant-free and surfactant-laden cases aligns with findings in Ref. [19], where bubble collapse times with surfactant could not be rescaled using t_c to match those in clean interfaces (see Fig. 2 of this reference). These observations, along with insights from Ref. [16] and the negligible influence of Oh on wave velocity [Fig. 3(a)], collectively suggest that Marangoni stresses—rather than lower overall surface tension—are the primary cause of delays and nonlinearity in capillary wave motion.

To conclude this section, it is pertinent to comment on the moments nearing the collapse singularity in surfactant-laden cases. In Figs. 5(k) and 5(l), we present our computed interfacial shapes for cases with insoluble surfactants across varying Bo, along with their scaled counterparts based on the self-similarity proposed in Ref. [14] [$h(r,t) \sim |t_0 - t|^{2/3}$, as discussed earlier in Figs. 3(d) and 3(e) for clean cases]. Interestingly, even in the presence of surfactant, we observe an almost perfect data collapse across time for each case below Bo = 5. This behavior can be explained as follows: the times displayed in the plots align with the valid temporal ranges reported in Ref. [14], corresponding to $T \gtrsim -0.1$. As can be seen in Fig. 5(j), the systems reach surfactant saturation at these comparative times, suggesting a local reduction (increase) in Oh (La) and bringing them much closer to the collapsing La range (1000–5000) reported in Ref. [14] compared to the clean cases.

Although our power-law fits offer a good representation of the $\tilde{\theta}$ data, we emphasize that the complex dynamics in the collapse vicinity preclude us from tracking the dominant capillary wave all the way to $\tilde{\theta} = 0$, complicating the examination of the final stages. As previously mentioned, the curvature reversal at the instant of jet ejection disrupts the system's self-similar behavior in clean cases as proposed in earlier works [12,14,45,46]. In surfactant-laden cases, we also expect major disruptions to our proposed power-law $\tilde{\theta}$ behavior as collapse is approached. In fact, we can infer a transition to a different regime, distinct from the power-law behavior, at $T \gtrsim -0.12$, given that that projections of the power-law fits to $\tilde{\theta} = 0$ do not match our recorded collapsing times in the simulations. For all cases, our recorded times fall behind those of the power-law projections, suggesting an acceleration of the dynamics. The authors recommend a thorough investigation of the moments very close to wave focusing and jet ejection ($\theta \approx 0$) in the presence of surfactants as an avenue for future research. Specifically, we recommend a focus on the "axe" shape adopted by the cavity as $\tilde{\theta} = 0$ is approached in the presence of surfactants, as seen previously in Refs. [17,19].

2. Effect of surfactant solubility and Marangoni stresses transition

Having dived into the general effects of surfactant addition, we now proceed to elucidate the effects of surfactant solubility and unveil the specific effects of Marangoni stresses on wave
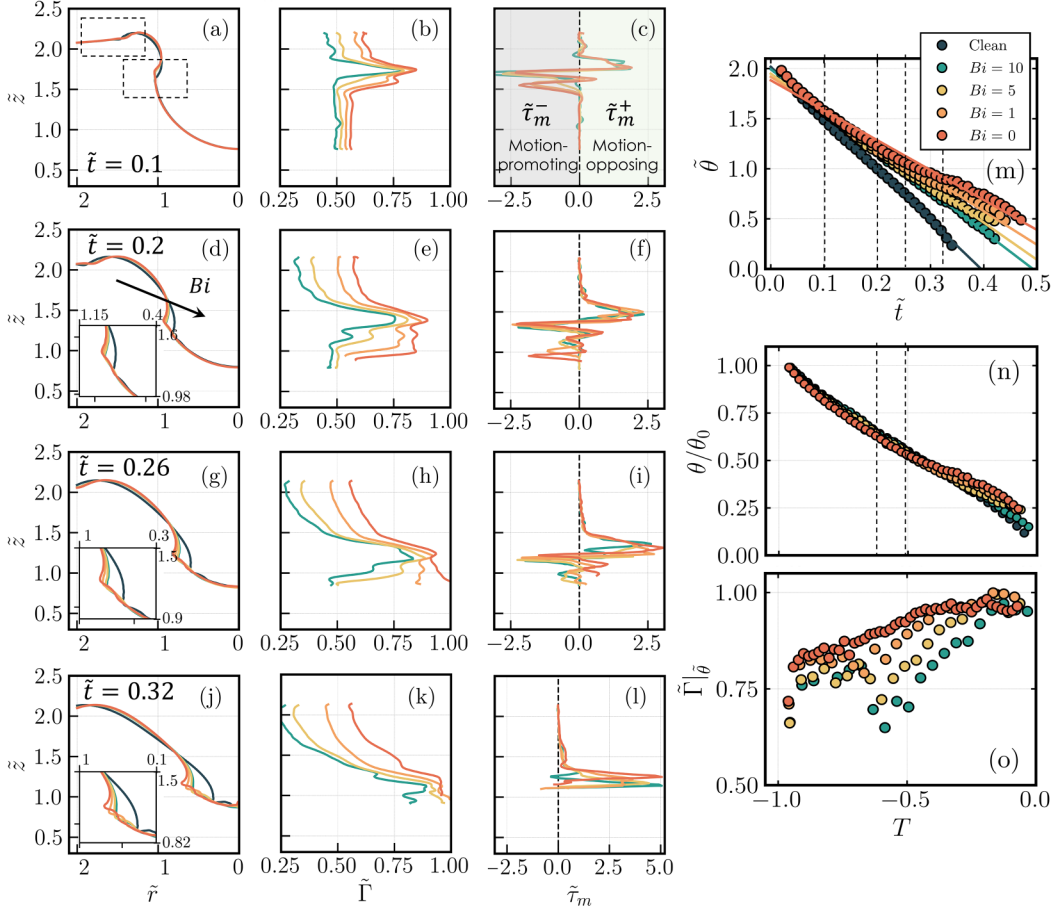
FIG. 6. Effect of surfactant solubility at $\beta_s = 0.3$ (Ma = 93.43) on capillary wave dynamics: (a), (d), (g), (j) interface shape, (b), (e), (h), (k) surfactant concentration along the interface, and (c), (f), (i), (l) Marangoni stresses along the interface. In (a)–(l), the abscissa represents the values of $\tilde{r}$, $\tilde{\Gamma}$, and $\tilde{\tau}_m$, shared across each column, and the ordinate represents the vertical coordinate, $\tilde{z}$, shared across all plots; (m) temporal evolution of $\tilde{\theta}$ wherein the vertical dashed lines correspond to the times depicted in (a)–(l); (n) data scaled by θ_0 and $\tilde{t}_0$; (o) interface surfactant concentration evaluated at the location of the dominant capillary wave. The markers represent our simulation data (taken every $\Delta\tilde{t} = 0.01$) and the lines correspond to a linear fit of the data for reference. For all cases in this figure, Bo = 0.5 and Oh = 3.21×10^{-3}.

propagation. Figures 6(a)–6(l) present a few snapshots of interface shape, $\tilde{\Gamma}$ profiles, and Marangoni stress profiles in the z direction, $\tilde{\tau}_m$, calculated via Eq. (10) for various Bi. Rows 1–4 in this series of plots represent different dimensionless times and columns 1–3 display projections of $\tilde{r}$, $\tilde{\Gamma}$, and $\tilde{\tau}_m$ (shown in the x axis) across the vertical axis, $\tilde{z}$ (shown in the y axis). We reiterate here that under our formulation, an increase in Bi signifies a higher likelihood of surfactant desorption into the bulk phase due to the smaller desorptive timescale compared to that of convection. Consequently, the Bi range is confined between a surfactant-free case (Bi $\rightarrow \infty$) and a fully insoluble surfactant (Bi = 0).

A clear monotonic trend regarding wave retardation and surfactant solubility is revealed, whereby lower Bi (lower solubility) cases consistently exhibit more pronounced delays in capillary wave motion in both the train evolving down the cavity and the one departing from it. A comparison of interfacial shapes at early ($\tilde{t} = 0.1$) and later ($\tilde{t} = 0.32$) bursting stages suggests that these delays intensify in time and that a distinct separation between surfactant and clean cases emerges over time.

This observation is consistent with those of Ref. [20], where even small surfactant concentrations (C/CMC $= 0.1$) were sufficient to actively alter the bursting dynamics. A measure of these delays is illustrated in Fig. 6(m), where progressively larger deviations from the linear behavior of the clean case arise as solubility is decreased. Similar to the insoluble cases at different Bo presented in Sec. III B 1, surfactant cases display noncollapsing dynamics against surfactant-free interfaces, as evidenced in Fig. 6(n). Despite the higher rates of surfactant desorption in larger Bi cases, reflected in the lower $\tilde{\Gamma}$ of the dominant wave at early and middle stages [Fig. 6(o), $T < -0.25$], it is interesting to note that all cases reach surfactant saturation near collapse ($\tilde{\Gamma} \to 1$). This is attributed to the much smaller interfacial areas involved in the temporal vicinity of collapse [see, for example, Fig. 13(b) at $T = 0$].

It is instructive to inspect the evolution of Marangoni stresses and surfactant concentration across the bubble's domain in the z direction. The $\tilde{\Gamma}$ peaks at early stages [$\tilde{t} = 0.1$–0.2; Figs. 6(b) and 6(e)], besides highlighting the location of the dominant wave, act as an important source of Marangoni stresses due to the generation of surface tension gradients [see Eq. (10)]. In our formulation, positive-signed Marangoni stresses projected onto the z direction ($\tilde{\tau}_m > 0$, denoted as $\tilde{\tau}_m^+$) are exerted in the positive z direction, diverting flow away from the bottom of the bubble and wave focusing point. In contrast, negative Marangoni stresses ($\tilde{\tau}_m < 0$, denoted as $\tilde{\tau}_m^-$) tend to pull the interface towards the focusing point at $\tilde{r} = 0$. Armed with these definitions, it is clear that the high-$\tilde{\Gamma}$ toroidal structure surrounding the dominant capillary wave engenders a complex interplay between positive and negative $\tilde{\tau}_m$, which retard and promote wave motion down the cavity, respectively. This is illustrated in Figs. 6(c), 6(f), and 6(i), in which two primary competing $\tilde{\tau}_m$ peaks are displayed. We henceforth refer to interfaces in this situation as subjected to "bidirectional" Marangoni stresses. As the system advances towards surfactant saturation in the region surrounding the collapsing point [$\tilde{t} = 0.32$; Figs. 6(j), 6(k), and 6(l)], the motion-promoting negative Marangoni stresses nearly vanish, leaving the interface exposed to strong motion-delaying positive Marangoni stresses (note the x-axis scale difference in the $\tilde{z}$ vs $\tilde{\tau}_m$ plots between $\tilde{t} = 0.32$ and the preceding times).

The emergence of bidirectional Marangoni stresses in the regions surrounding a capillary wave has also been observed in the context of surfactant-laden plunging breakers. As shown in Fig. 5(a) of Ref. [48], there is a leap from low $\Delta\sigma/\Delta A$ ($|\tilde{\tau}m| = 0$) to high $\Delta\sigma/\Delta A$ ($|\tilde{\tau}m| > 0$) near the point of maximum curvature, and back to low $\Delta\sigma/\Delta A$ [see Fig. 6(c)].

The mechanism outlined above elucidates what the authors define as a transition from bidirectional to unidirectional Marangoni stresses, a pivotal factor in the observed retardation of capillary waves on surfactant-laden bursting bubbles, as documented in this and prior studies. A visual depiction of this transition is provided in Figs. 4(a)–4(d). As shown in Fig. 6(n), the magnitude of motion-delaying positive Marangoni stresses appears to overcome that of motion-promoting negative stresses within the time interval $\tilde{t} = 0.20$–0.26. This critical period is demarcated by the corresponding vertical dashed lines in Fig. 6(m), marking the juncture where the $\tilde{\theta}$ vs $\tilde{t}$ data for Bi $= 0$ begin to diverge markedly from the behavior observed in surfactant-free cases. In the scaled space outlined by θ/θ_0 and T in Fig. 6(n), these times correspond to $T \approx [-0.60, -0.50]$ for Bi $= 0$, also coinciding with the onset of significant noncollapsing behavior.

3. Effect of surfactant elasticity and capillary wave velocity compilation

In this section, we illustrate the impact of surface elasticity, denoted by β_s, on wave propagation. Additionally, we present an analysis of the combined effects of Bi and β_s on average capillary wave velocity, $|\tilde{u}_\theta|$, across varying Bo values. As explained in Sec. II A, β_s characterizes the sensitivity of surface tension to surfactant concentration, as expressed in Eq. (8). It also quantifies the strength of Marangoni stresses, as shown in Eq. (10), the Marangoni modulus [27], and the Marangoni number Ma, as seen in Eq. (11). Ma provides a dimensional measure of the significance of Marangoni stresses relative to viscous stresses. Figure 7(a) provides a comparison of the temporal evolution of $\tilde{\theta}$ for different values of β_s, with the surfactant-free case denoted as $\beta_s = 0$. Sample snapshots of the interface shape are also shown in Figs. 7(d) and 7(g). As anticipated, an increment
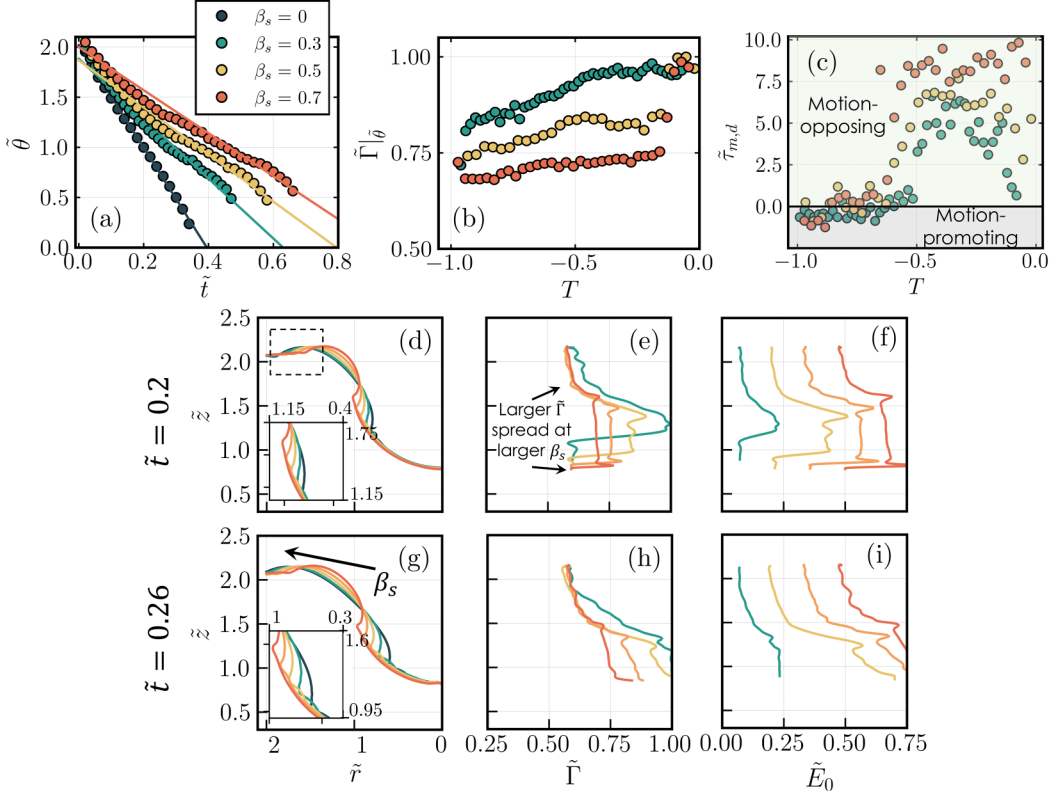
FIG. 7. Effect of surfactant elasticity at Bi $= 0$ in the range $\beta_s = 0.3$–0.7 (Ma $= 93.43$–218.01) on capillary wave dynamics: (a) temporal evolution of $\tilde{\theta}$; (b) interface surfactant concentration evaluated at the location of the dominant capillary wave, scaled temporarily by the comparative time; (c) magnitude difference of positive (motion-opposing) and negative (motion-promoting) Marangoni stress peaks across the interface. The markers represent our simulation data (taken every $\Delta\tilde{t} = 0.02$) and the lines correspond to a linear fit of the data for reference; (d)–(i) sample interface shapes, surfactant concentrations, and Marangoni moduli along the interface at $\tilde{t} = 0.2$ for (d)–(f) and $\tilde{t} = 0.26$ for (g)–(i). In (d)–(i), the abscissa represents the values of $\tilde{r}$, $\tilde{\Gamma}$, and $\tilde{E}_0 = E_0/\sigma_s$ and the ordinate represents the vertical coordinate, $\tilde{z}$, shared across all plots. For all cases in this figure, Bo $= 0.5$ and Oh $= 3.21 \times 10^{-3}$.

in β_s yields a positive, monotonic response in terms of wave motion retardation. Similar delays in capillary-related events with increased surfactant elasticity have been documented in previous studies concerning liquid thread retraction or breakup [31,49], ink-jet printing [50], drop impact [51], and bubble motion in capillary channels [36].

It is interesting to note that the condition with the most pronounced wave delay (i.e., $\beta_s = 0.7$, Ma $= 218$) does not align with the one exhibiting the highest $\tilde{\Gamma}$ at the dominant wave location at the same comparative time [refer to Fig. 7(b)]. Similarly, it does not correspond to the largest $\tilde{\Gamma}$ in the toroidal region formed in the vicinity of the dominant wave, as seen in Figs. 7(e) and 7(h). This contrasts with the dynamics explored in our examination of Bi, where the case yielding the greatest delays (Bi $= 0$, insoluble surfactant) always corresponded to the highest $\tilde{\Gamma}$ at the dominant wave and its surrounding regions [refer to Figs. 6(b), 6(e), 6(h), 6(k), and 6(o)]. This is easily explained by recalling the fact that an increase in β_s is accompanied by an increase in Marangoni stresses strength relative to viscous stresses (larger Ma). These stresses promptly redistribute $\tilde{\Gamma}$ across the interface, forming a larger surfactant "spread" near the dominant wave, leading to localized lower $\tilde{\Gamma}$ at larger β_s.
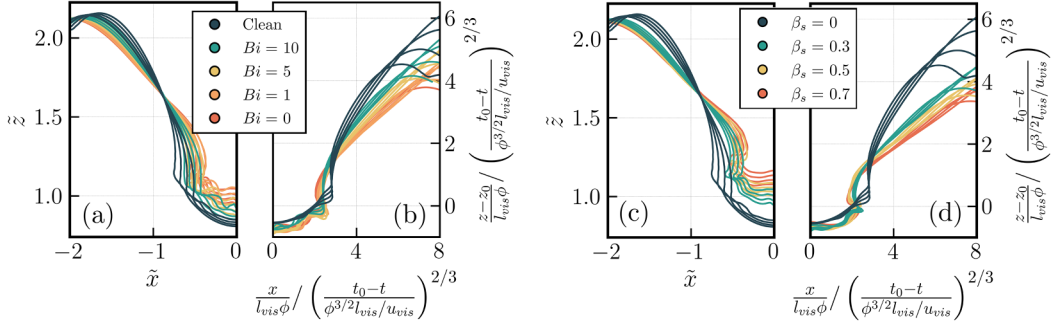
FIG. 8. Interface collapse under varying Bi and β_s conditions according to the scaling proposed in Ref. [14] in the range $t_0 - t \approx 6t_{pre} - 10t_{pre}$; z_0 represents the point in the vertical coordinate where jet ejection occurred; (a) and (b) effect of Bi at constant $\beta_s = 0.3$ (Ma $= 93.43$); (c) and (d) effect of β_s in the range $\beta_s = 0.3–0.7$ (Ma $= 93.43–218.01$) at constant Bi $= 0$. The clean case in (c) and (d) is denoted by $\beta_s = 0$. For these cases, Oh $= 3.21 \times 10^{-3}$ and Bo $= 0.5$.

Increased β_s values lead to greater interfacial resistance to compression, as demonstrated by the consistently larger Marangoni elasticity E_0 profiles in Figs. 7(f)–7(i) (see the end of Sec. II A for the definition of E_0). This resistance, due to surface-active contaminants, is well known to be associated with interface rigidification and reduced interfacial velocity, as previously demonstrated in bursting bubbles [16] and other scenarios [34,35]. This phenomenon further elucidates the observed bubble collapse retardation at higher β_s values (higher Ma).

The preceding discussion offers a direct link to why larger values of β_s precipitate lower wave propagation velocities. Illustrated in Fig. 7(c), we present our computations of the magnitude difference between the peaks of positive (motion-opposing) and negative (motion-promoting) Marangoni stresses in the z direction at the beginning and end of the high-$\tilde{\Gamma}$ toroidal structure, denoted as $\tilde{\tau}_{m,d} = |\tilde{\tau}_m^+| - |\tilde{\tau}_m^-|$. This parameter serves as a measure of the collective influence of Marangoni stresses within the system, with positive $\tilde{\tau}_{m,d}$ instigating overall wave motion retardation down the cavity. As depicted in Fig. 7(c), the time interval $T \approx [-0.75, -0.60]$ marks the juncture where motion-delaying stresses prevail over their motion-promoting counterparts as a whole. In this figure one can also see that the largest β_s case consistently experiences the largest $\tilde{\tau}_{m,d}$ after $T \approx [-0.75, -0.60]$, confirming the presence of overall stronger motion-delaying Marangoni stresses and explaining the lower average wave velocities obtained for larger β_s and their more pronounced departures from linearity.

In Fig. 8, we illustrate the effects of Bi and β_s at constant Bo $= 5$ and Oh $= 3.21 \times 10^{-3}$ on the universal interfacial shape profiles proposed in Ref. [14]. As discussed in Figs. 3(d), 3(e), 5(k), and 5(l), a significant distinction is observed between the uncontaminated case (dark green) and the surfactant cases. This disparity is particularly noticeable in the β_s plot in rescaled space, where the profiles for $\beta_s = 0.3–0.7$ collapse reasonably well over time and among themselves, contrasting sharply with the clean case which stands out as an outlier. As previously noted, the regions surrounding the bottom of the cavity in surfactant cases exhibit much larger Oh values due to reduced surface tension, bringing the system closer to bursting conditions for which the scaling of Ref. [14] was originally proposed. As demonstrated in Figs. 6(a)–6(l) and 7(d)–7(i), Marangoni stresses, though significant in magnitude at these time points [see Fig. 7(c) for $T > -0.1$], primarily manifest upstream from the bubble's dominant wave, suggesting a Marangoni-free zone at the cavity's bottom and elucidating the better collapse observed in surfactant cases. We note here that the semicollapsed interface profiles shown in Fig. 8 correspond to times close to the bubble collapse singularity ($T > -0.1$), whose dynamics differ from the behavior of $\tilde{\theta}$ vs $\tilde{t}$ discussed earlier. The aforementioned nonlinearity in the propagation of the dominant capillary wave in surfactant cases, across various Bi values [see Fig. 6(m)] and β_s values [see Fig. 7(a)], is further elucidated in

TABLE II. Effect of Bi (at constant $\beta_s = 0.3$) and β_s (at constant Bi $= 0$) on the exponent of a power-law fit of the form $\tilde{\theta} \sim \tilde{t}^\alpha$ of the $\tilde{\theta}$ vs $\tilde{t}$ data [see Figs. 6(m) and 7(a)]. For all cases displayed in the table, Bo $= 0.5$ and Oh $= 3.21 \times 10^{-3}$.

Bi	$|\tilde{u}_\theta|$	$|\tilde{u}_{\theta,\text{lin}}|$	α	β_s (Ma)	$|\tilde{u}_\theta|$	$|\tilde{u}_{\theta,\text{lin}}|$	α
10	3.866	4.047	0.868	0.1 (31.15)	3.774	3.585	0.6
5	3.747	3.716	0.729	0.3 (93.43)	3.315	2.987	0.587
1	3.499	3.354	0.637	0.5 (155.76)	2.837	2.348	0.5936
0	3.315	2.987	0.587	0.7 (218.07)	2.433	2.143	0.559

Table II. Upon examining this and Table I, which illustrates the influence of Bo on the exponent of the power-law fit $\tilde{\theta} \sim \tilde{t}^\alpha$, it is evident that α increases with Bo, which signifies a closer behavior to that of clean interfaces for larger, more deformable bubbles. In the case of increasing β_s, the value of α reduces to that associated with weakly deformable bubbles characterized by vanishingly small Bi (insoluble cases). This is consistent with the fact that surfactant-induced Marangoni stresses counteract the propagation of the waves and act to rigidify the interface.

We conclude our exploration of the precollapse dynamics by presenting an extended sweep of Bi and β_s in Figs. 9(a) and 9(b), which illustrates the intertwined influence of these surfactant parameters on the average wave velocity, $|\tilde{u}_\theta|$, across varying Bo conditions. It is relevant to reiterate that $|\tilde{u}_\theta|$ represents the *average* velocity computed over time for each case, acknowledging the previously discussed nonlinear nature of $\tilde{\theta}$ vs $\tilde{t}$ in surfactant-laden cases. Our extended parametric sweep confirms that the distinct monotonic effects of Bi and β_s elucidated previously persist up to our highest Bo tested (Bo $= 5$). Specifically, we observe that $|\tilde{u}_\theta|$ exhibits a negative response (i.e., motion retardation) to a decrease in Bi (less soluble surfactant) or an increase in βs ("stronger" surfactant) for all Bo.

As previously discussed, the dependence of $|\tilde{u}_\theta|$ on Bi and β_s can be attributed to the significant increase in motion-delaying Marangoni stresses observed with decreasing Bi or increasing β_s [see, for example, Fig. 7(c)]. We highlight, however, that these heightened stresses, which directly correlate with $\nabla_s \tilde{\Gamma}$ and β_s [refer to Eq. (10)], are manifested differently for Bi and β_s. In cases
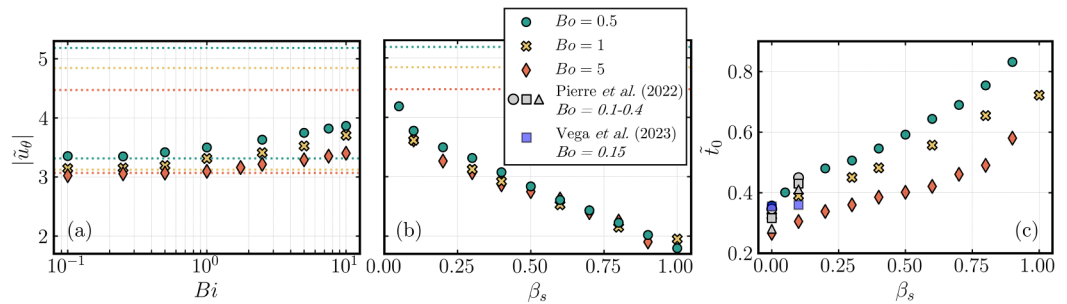

FIG. 9. Compilation of Bi and β_s effects on average dominant capillary wave velocity and collapse time under varying Bo conditions: (a) effect of Bi on $|\tilde{u}_\theta|$ at constant $\beta_s = 0.3$ (Ma $= 93.43$); (b) effect of β_s on $|\tilde{u}_\theta|$ at constant Bi $= 0$. The dotted lines in (a) represent the average velocity of each Bo for the clean case (top lines, Bi $\to \infty$) and insoluble surfactant (bottom lines, Bi $= 0$). The dotted lines in (b) represent the average velocity of each Bo for the clean case ($\beta_s = 0$). For all cases in (a) and (b), Oh $= 3.21 \times 10^{-3}$; (c) effect of β_s in the range $\beta_s = 0.05$–1 (Ma $= 15$–311) at constant Bi $= 0$ on collapse time and comparison against the experimental measurements of Refs. [19,20] (Oh $\sim O(10^{-3})$) at an equivalent equilibrium concentration $C/\text{CMC} \approx 0.25$. The markers representing Pierre *et al.*'s [19] data correspond to circles for Bo ≈ 0.1, squares for Bo ≈ 0.17, and triangles for Bo ≈ 0.40.

of decreased Bi, the higher $\nabla_s \tilde{\Gamma}$ at the start and end of the toroidal structure carrying the dominant wave induces the generation of larger Marangoni stresses compared to cases with larger Bi [see Fig. 6(k)]. Conversely, as β_s increases, it is the greater magnitude of β_s itself, rather than larger surface tension gradients at the toroidal structure, $\nabla_s \tilde{\Gamma}$, that leads to larger Marangoni stresses. As illustrated by the identical ordinate range of the plots in Figs. 9(a) and 9(b), $|\tilde{u}_\theta|$ appears to be consistently more sensitive to variations in Bo across the tested range of Bi compared to β_s. This trend suggests that the influence of β_s overwhelmingly dominates that of Bo. The non-negligible Bo effects across our Bi range align with the initial surfactant concentration effects on collapse time revealed experimentally by Ref. [20].

Figure 9(c) compares our dimensionless collapse times with experimental data from Refs. [19,20], demonstrating that our results align well within the ranges reported in these studies for both surfactant-free (shown as $\beta_s = 0$) and surfactant-laden cases (shown as $\beta_s = 0.1$) under similar conditions of Oh and Bo. Both referenced studies utilize SDS, an insoluble surfactant, and provide data at varying initial surfactant concentrations. To ensure compatibility with our study, we used the interfacial tension isotherm relating σ to Γ from Refs. [20,52] and fitted it to the Langmuir expression [Eq. (8)]. This fitting yielded $\beta_s \approx 0.1$, consistent with other reports for SDS [53] and other common surfactants like Triton X-100 [33]. Considering our constant initial surfactant concentration of $\tilde{\Gamma}_0 = 0.55$, the approximately equivalent bulk concentration is $C/\text{CMC} = 0.25$, as derived from the Γ vs C/CMC data in Ref. [20] [see Fig. 2(b) of this reference]. Since the lowest C/CMC reported in Ref. [19] is approximately 0.25, we present values from both references at this concentration.

C. Contaminated interfaces: Jet drops and aerosol release

We now focus briefly on the Worthington jet and the process of surfactant enrichment during collapse and jet breakup. As remarked in our Introduction, recent works [8,9] have proposed that the jet ejection phenomenon following cavity collapse is primarily driven by inertia, with viscosity playing a modulating role, rather than by an inertiocapillary mechanism. Figures 10(a)–10(h) present a few snapshots of postcollapse interfacial shape and pressure contours for a surfactant-free (left half) and an insoluble surfactant case (right half). The parameters for these cases are identical to those in Fig. 4. We highlight that these snapshots are taken at the same temporal distance from collapse and hence the visualizations represent the true differences between cases at the same stages of development. To complement these visualizations, we include plots of maximal interface location in the z direction as a function of our comparative time for multiple Bo and β_s in Figs. 10(i)–10(l). As mentioned in our discussion of Fig. 13(d) in Appendix B, $\tilde{z}_{\max}$ serves as a proxy for the location of the jet or first released drop.

Building upon the insights from Sec. III B, the observations from Figs. 6(o) and 7(b), alongside previous work [16], demonstrate that surfactant concentration approaches saturation close to the moment of cavity collapse under our studied set of Bi, β_s, and Bo. This critical observation lays the foundation for the emergence of Worthington jets in areas marked by high $\tilde{\Gamma}$, which, as a result, exhibit significantly larger local Oh compared to cases devoid of surfactant contamination. Invoking the jet ejection velocity scalings proposed and validated by Refs. [8,9], $\tilde{u}_{\text{jet}} \sim \text{Oh}^{1/2}$ for Oh < 0.043, or those of Ref. [13], $\tilde{u}_{\text{jet}} \sim \text{Oh}^{1/2}(\text{Oh}_* - \text{Oh})^{-3/4}$ $(\text{Oh}_* = 0.043)$, it is therefore expected that the addition of surfactant increases the dimensionless jet ejection velocity. This is evidenced qualitatively during the first few postcollapse stages in Figs. 10(a)–10(c) $(T < 0.18)$, where the tip of the surfactant-covered jet consistently exceeds the vertical location of the surfactant-free jet. Examining the insets of Figs. 10(i)–10(k), with the horizontal dashed line representing the location of the liquid pool-atmosphere interface $(\tilde{z} = 2)$ and the vertical line the bubble collapse time, it is clear that between the surfactant-free and surfactant-covered jet, it is the latter that first surpasses $\tilde{z} = 2$, suggesting a larger ejection velocity. Additional discussions on how jet and first detached drop velocities in contaminated scenarios compare to uncontaminated systems can be found in Appendix A [Fig. 12(e)].
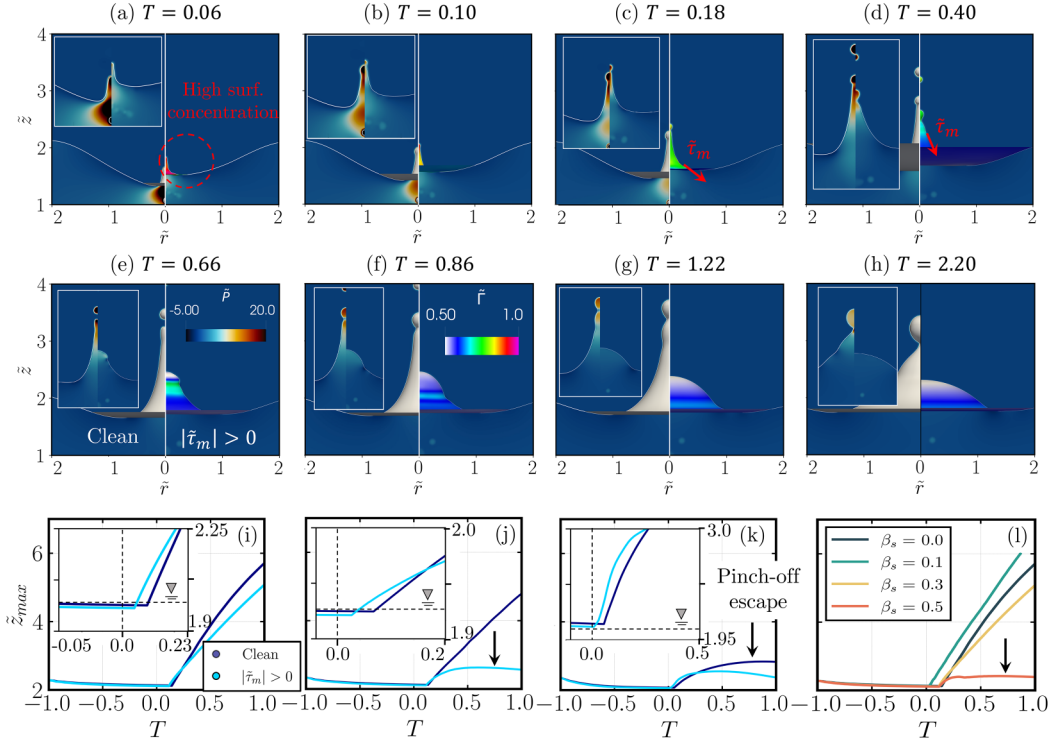
FIG. 10. Effect of insoluble ($\mathrm{Bi} = 0$) surfactant on Worthington jet dynamics: (a)–(h) comparison of temporal evolution (at the same T) of interface shape and pressure fields for surfactant-free interfaces on the left half and insoluble surfactant on the right half; the operating conditions for both the clean and surfactant case are identical to those in Fig. 4. The insets focus on the emerging jet's pressure fields, while the dashed red circle focuses on the jet's near surfactant saturation at early jetting stages. The red arrows schematically indicate the primary direction of Marangoni stresses; (i)–(k) temporal evolution of maximal vertical location of the interface for $\mathrm{Bo} = 0.5, 1, 5$, respectively; (l) effect of β_s at $\mathrm{Bo} = 0.5$. The black arrows point to instances of pinch-off escape.

The authors of Ref. [19] have documented much larger jet velocities generated by surfactant-laden bursting bubbles prior to the first pinch-off event. Interestingly, our results after these first ejection stages [$T > 0.18$, Figs. 10(d)–10(h)] uncover a complete trend reversal in terms of jet velocity and shape. While the surfactant-free jet continues to grow and undergo pinch-off events up until $T \approx 1.22$, the contaminated jet quickly reaches its maximum length at $T \approx 0.40$ and proceeds to drain out, leading to the thick, interfacially rigid structure shown at $T = 2.20$. These findings can be rationalized by incorporating the effects of Marangoni stresses into our analysis. As the jet grows in size and interfacial area surges after t_0, surface tension gradients arise across the jet's domain, resisting the positive pressure gradient pushing the jet upwards and prompting interfacial stabilization. This is schematically shown by the red arrows in the contour plots. An in-depth showcase of the Marangoni stresses profile along the Worthington jet can be found in Ref. [16]. While this paper attributes the lower jet velocity at later times to Marangoni stresses opposing the direction of growth, it is important to note that surfactant-laden systems in real-life scenarios may also exhibit additional rigidification and viscosity-related effects due to surface viscoelasticity [27]. Considering these additional dynamics alongside purely Marangoni effects may help reconcile measurements in surfactant-laden cases with those of clean interfaces; we suggest this topic as an avenue for future research.

The variations in $\tilde{z}_{\max}$ resulting from changes in β_s [Fig. 10(l)] are a testament of the complex dynamics underpinning surfactant-laden bursting bubbles. In the case of $\beta_s = 0.1$, not only does the jet ejection velocity surpass that of the surfactant-free case, but its first ejected drop maintains this higher velocity throughout the entire temporal span. The above suggests that there exist situations in which Marangoni stresses originated from very weak surfactants cannot override the lowered capillary resistance to jet growth or breakup (larger local Oh) caused by the surfactant presence. Similar intricate surfactant behaviors have been reported in Ref. [36].

In addition to jet velocity and size, surfactant contamination severely disrupts the capillary breakup dynamics of the Worthington jets. As is well known in the literature across a wide array of fluid mechanics problems (see, for instance, Refs. [31,33,36,49,54–59]), Marangoni stresses, rather than reduced local surface tension, play a primary role in seeking to reopen the capillary neck, thereby resisting end pinching. In the context of bursting bubbles, this either dramatically reduces the number of ejected drops or completely inhibits the capillary singularity, as highlighted by the black arrows in Figs. 10(j)–10(l). In these cases, the combination of Marangoni-driven end-pinching resistance and the stabilizing action of gravitational forces discussed in Sec. III A completely preclude the jet from pinching. We relate the aforementioned Marangoni-driven phenomenon to the "escape from pinch-off" mechanism in isolated liquid threads described by Refs. [31,56], wherein neck reopening is attributed to the detachment and advection of a vortex ring towards the bulk of the forming bulbous tip.

To conclude our discussion, we delve into the process of contamination enrichment of aerosol drops. As demonstrated in previous investigations [60], any type of contamination in the liquid bulk can have highly problematic consequences due to the accumulation of these contaminants—oftentimes environmentally harmful—in the drops released to the atmosphere. Although the focus of this study comprised situations in which drop release is heavily suppressed, a few insights can be gathered from our simulations. Taking our base surfactant-free case, characterized by $Oh = 3.21 \times 10^{-3}$ and $Bo = 0.5$, a total of three ejected drops were obtained, with their radii relative to the bubble radius being $R_{d,i}/R_0 = 7.7\%$, 9.42%, and 21.3%, respectively (i denotes the order of ejection). We note that the size of the first ejected drop agrees well with the reports of Ref. [61] ($R_{d,1}/R_0 \approx 6\%$). In contrast, the sole drop produced by an insoluble surfactant at the same Bo and a moderate $\beta_s = 0.3$ exhibited a size of $R_{d,1}/R_0 = 4.9\%$ and showed significant enrichment in terms of both interface and bulk surfactant concentration. Specifically, taking the surface average of Γ and the volume average of C within the drop, we obtain $\Gamma_{d,1}/\Gamma_0 = 145.4\%$ and $C_{d,1}/C_\infty = 774.4\%$. This striking surfactant enrichment (≈ 1.5–8 times the initial values) is within the range of experimental enrichment factors of particulate and bacterial contaminants reported in Refs. [27,61,62].

IV. CONCLUDING REMARKS

We have dived into the classic phenomenon of bubbles bursting through a liquid-gas interface via numerical simulations, exploring two scenarios that, despite their practical significance, have only recently garnered attention: surface-active contamination and non-negligible gravitational forces compared to capillary forces, characterized by large Bond numbers, $Bo \gg 10^{-3}$. Building upon the recent experimental [17,19,20] and numerical [16] work centered around surfactant effects on bursting bubble dynamics, our simulations have allowed us to provide detailed quantitative insights about the system. These include the temporal evolution of the dominant capillary wave angular location as it traverses down the cavity before collapse ($\tilde{\theta}$ vs $\tilde{t}$), an exploration of the self-similarity of interfacial shape, Worthington jet growth, surfactant concentration, and Marangoni stress profiles along the interface, and the collective impact of surfactant parameters on these variables. This information is notably challenging to access experimentally. Herein, we have also proposed a phenomenological mechanism that explains the capillary wave retardation reported experimentally and numerically in surfactant-laden bursting bubbles.

Gravitational effects were found to be relevant in uncontaminated interfaces in terms of average velocity of the capillary wave, $|\tilde{u}_\theta|$, at large Bo. Prior investigations [10] had reported insignificant variations in $|\tilde{u}_\theta|$ with Bo for Bo < 0.7. Nonetheless, our study, which extended the examined Bond number range up to Bo = 5, reveals small but non-negligible decreases in $|\tilde{u}_\theta|$ with Bo for our Oh range considered, $1\times10^{-3} <$ Oh $< 1\times10^{-2}$, suggesting a power-law fitting of the form $|\tilde{u}_\theta| \sim -$Bo. We have attributed the negative response of $|\tilde{u}_\theta|$ to Bo to the much larger pressure gradients between the depths of the liquid pool and the areas surrounding the bubble at larger Bo, which compete with capillary wave motion and stabilize the system. In line with previous work for Bo $\rightarrow O(10^{-3})$ [8,9], our extended Bo range has confirmed that alterations in Oh do not produce variations in $|\tilde{u}_\theta|$, even at Bo = 5.

An important conclusion that can be drawn from this investigation corresponds to the substantially different prebubble collapse phenomena that emerge as surfactant is introduced to the system. Previous investigations, alongside our present research, have demonstrated that $\tilde{\theta}$ vs $\tilde{t}$ behaves linearly in interfaces devoid of surfactant, implying constant $|\tilde{u}_\theta|$. Our simulations have revealed that Marangoni stresses, generated by nonhomogeneous surface tension distributions, not only delay wave motion by about 30–70%, but also completely disrupt the linearity of $\tilde{\theta}$ vs $\tilde{t}$. For insoluble surfactants, dominant capillary wave motion was found to lean closer to $\tilde{\theta} \sim \tilde{t}^\alpha$, with $\alpha = 0.45$–0.70, depending on Bo. We note, however, that the dominant capillary wave undergoes a behavioral transition close to the instant of collapse, briefly exhibiting motion acceleration. A comprehensive examination of the moments leading up to bubble collapse is left for future work.

Throughout this investigation we have introduced a mechanism that rationalizes the delays in wave motion induced by surfactants, involving the transition from primarily "bidirectional" to primarily "unidirectional" Marangoni stresses. This mechanism can be summarized as follows. The large curvature that accompanies the surrounding areas of the dominant wave generates a toroidal region covered with surfactant [see Fig. 4(a)] from which "downwards" ($\tilde{\tau}_m < 0$, motion-promoting) and "upwards" ($\tilde{\tau}_m > 0$, motion-opposing) Marangoni stresses emerge. As collapse is approached, surfactant saturation at the bottom of the bubble [see Fig. 4(c)] eliminates $\tilde{\tau}_m < 0$, subjecting the interface to strong, unidirectional stresses heavily opposing wave motion across the cavity. This work has also presented a parametric sweep of two dimensionless groups relevant to various types of surfactants: surfactant solubility, given by Bi, and surfactant strength, given by β_s. The former quantifies the rate at which surfactant desorbs into the liquid bulk phase while the latter is a proxy for the strength of Marangoni stresses. More pronounced reductions in capillary wave velocity were found for surfactants featuring weaker solubility (lower Bi) and larger β_s. This trend is explained by larger Marangoni stresses prompted by smaller Bi and larger β_s.

Finally, this study has complemented the numerical observations of Refs. [16,19] regarding surfactant effects on the Worthington jet. The unequivocally larger local Oh close to the bubble collapse point brings about larger jet ejection velocities in surfactant cases, in line with the well-established scalings proposed in previous works for clean interfaces [8,13]. Nevertheless, jet expansion and growth force the emergence of strong Marangoni stresses that resist interfacial elongation and jet breakup via the Rayleigh-Plateau instability, ultimately leading to low-velocity jets and a significantly reduced number of ejected drops.

This investigation provides additional evidence to underscore the profound impact of surface-active contaminants, which are ubiquitous in nature, on the dynamics of bursting bubbles throughout the pre- and postcollapse stages. These effects extend beyond the mere retardation of bubble collapse, influencing the size distribution and degree of contamination of aerosol drops. For future research, the authors recommend an in-depth numerical and experimental exploration of surface rheological effects with surfactants, which are believed to significantly influence bursting bubbles, as indicated by the experiments of Refs. [17]. Of particular interest is the behavior of the jet, from ejection to drop detachment, and the isolation of Marangoni-driven mechanisms from those emerging due to surface rheology.
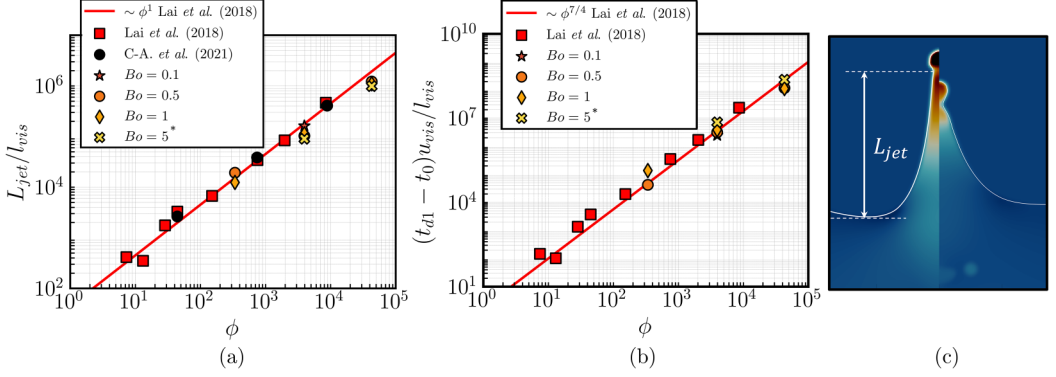
FIG. 11. Comparison of our surfactant-free simulations for varying Bo and La against the scaling (red lines) and numerical simulations (red squares) of Lai *et al.* [14] and the numerical data of Constante-Amores *et al.* [16] at Bo $\sim O(10^{-3})$ (black circles) using our same numerical approach: (a) dimensionless jet length before first drop detachment, $L_{\text{jet}}/l_{\text{vis}}$; (b) dimensionless temporal distance between cavity collapse and first detachment, $(t_{d1} - t_0)u_{\text{vis}}/l_{\text{vis}}$; (c) schematic representation of how $L_{\text{jet}}/l_{\text{vis}}$ is measured. Asterisk denotes measurements at the point of largest L_{jet} attained for Bo = 5 given the complete escape from pinch-off.

ACKNOWLEDGMENTS

APPENDIX A: CODE VALIDATION AND DROP SIZE AND VELOCITY IN THE PRESENCE OF SURFACTANT

Due to the inherent complexity of bursting bubbles and their associated features, it is crucial to ensure that our numerical method and setup correctly recover the well-documented bursting behavior at different stages. In Fig. 11, we present our surfactant-free numerical results across different Bo and La conditions, comparing them with the scaling laws proposed by Lai *et al.* [14] for two key parameters: jet length before first drop detachment, L_{jet}, and the temporal interval between first detachment, t_{d1}, and bubble collapse, t_0. These variables are made dimensionless by the viscous length and timescales (l_{vis} and $t_{\text{vis}} \equiv l_{\text{vis}}/u_{\text{vis}}$, respectively); the x-axis variable, ϕ, is defined in Eqs. (A1):

$$L_{\text{vis}} = \frac{\mu_l^2}{\rho_l \sigma_s}, \quad t_{\text{vis}} = \frac{\mu_l^3}{\rho_l \sigma_s^2}, \quad l_{\text{vis}} = \frac{\mu_l^2}{\rho_l \sigma_s}, \quad u_{\text{vis}} = \frac{\sigma_s}{\mu_l},$$

$$\phi = \text{La}(\text{La}_*^{-1/2} - \text{La}^{-1/2}) = \text{Oh}^{-2}(\text{Oh}_* - \text{Oh}). \tag{A1}$$
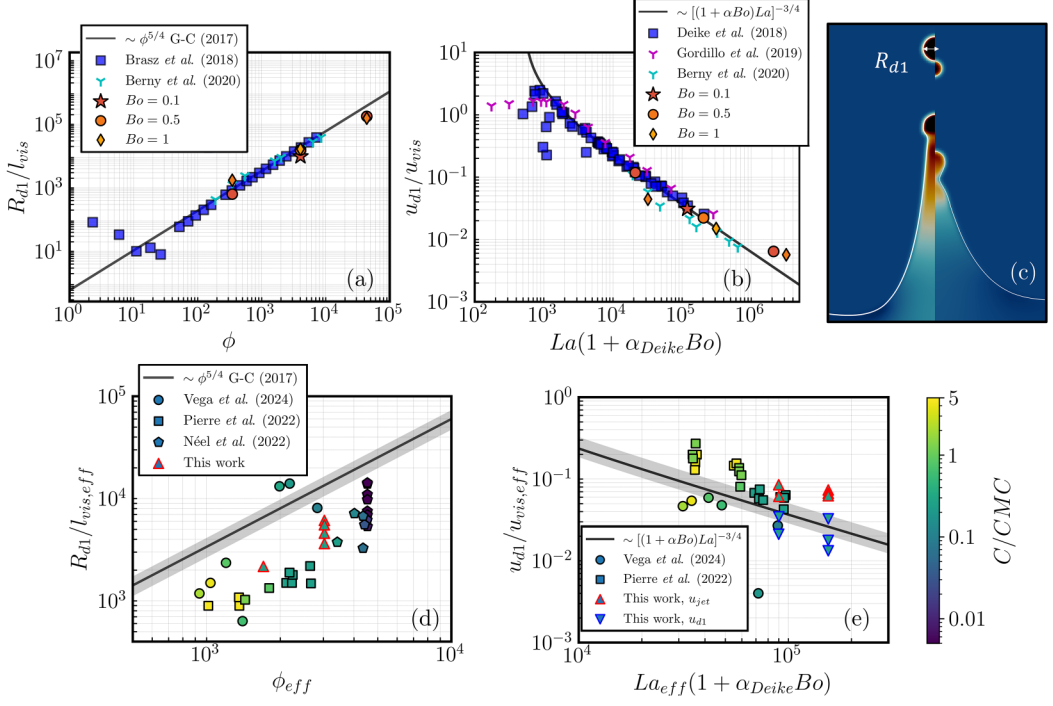
FIG. 12. Comparison of the dynamics of the first released drop obtained with our (a) and (b) surfactant-free and (d) and (e) surfactant-laden simulations against previous work: (a) scaling for dimensionless drop size, R_{d1}/l_{vis}, proposed by Gañán-Calvo [13] (black line); (b) Bo-dependent scaling for dimensionless drop velocity, u_{d1}/u_{vis}, proposed by Deike *et al.* [4] (black line). Here, $\alpha_{Deike} = 2.2$; (c) schematic representation of R_{d1}; (d) and (e) first released drop size and velocity in surfactant systems against SDS literature under varying C/CMC conditions. The shaded grey area portrays the dispersion of experimental data in surfactant-free systems, amounting to ≈20%. The points from Vega and Montanero [20] are at Bo ≈ 0.13–0.16, those from Pierre *et al.* [19] are at Bo ≈ 0.1–0.4, and those from Néel *et al.* [18] are at Bo ≈ 0.4. Our points represented by triangles in (e) denote jet ejection velocity, whereas inverted triangles denote first ejection velocity. The surfactant conditions shown in the plot are Bo = 0.1, 0.5, Bi = 0, 5, and $\beta_s = 0.3, 0.7$.

In the above, $La_* \approx 500$ denotes the critical value below which no drop detachment is observed as Bo → 0. As depicted in Fig. 11, our simulation results exhibit favorable agreement with prior numerical and theoretical investigations. The minor deviations observed in terms of L_{jet} with increasing Bo indicate the presence of subtle but non-negligible gravitational effects beyond Bo ≈ 1, impeding jet growth before the first detachment. In Sec. III A, we analyze the implications of these small effects, which become increasingly pronounced following initial detachment.

We complement our validation by examining the size, R_{d1}, and velocity, u_{d1}, of the first ejected drop in surfactant-free interfaces in Figs. 12(b) and 12(c). Drop sizes are compared against the scaling proposed by Gañán-Calvo [13], while velocities are assessed against Deike *et al.*'s [4] extension of Gañán-Calvo's [13] original law to include the effects of Bo. We also incorporate a few numerical and experimental results from previous investigations in the figures. In particular, we include the experimental measurements of R_{d1} by Brasz *et al.* [11] at Bo = 0–1 and the numerical results reported in Ref. [41] at Bo = 1. For u_{d1}, we display the results of Gordillo and Rodríguez-Rodríguez [8] at Bo = 5×10^{-1}, those of Deike *et al.* [4] at Bo = 10^{-3}–0.5, and those of Berny *et al.* [41] at Bo = 1. As discussed in Sec. I, R_{d1} and u_{d1} have been extensively investigated, resulting in a substantial body of numerical and experimental data validating the proposed scalings.

Our figure includes a select set of data under conditions similar to ours for reference, but we encourage readers to consult Refs. [1,2,10,12,63–65] for additional data points.

Ejected drop and Worthington jet velocities have been a subject of considerable debate, primarily due to measurement inconsistencies across different studies. In Ref. [4], velocities are measured at the instant before jet breakup, when the jet has stabilized at a constant vertical velocity. This definition deviates from the approach of Gordillo and Blanco-Rodríguez [9] and collaborators, where the jet's velocity at its very inception is the variable considered and related to La. Others [1] perform their measurements at the moment the jet crosses the liquid pool-atmosphere interface. These inconsistencies explain why, for instance, Gordillo and Rodríguez-Rodríguez's [8] velocities in our plot are generally larger than Deike *et al.*'s [4], even at similar Bo. By adhering to the latter reference's definition, we demonstrate how our simulations align well with the scalings observed in previous work. The point corresponding to La $= 10^4$ [shown as La$(1 + \alpha_{\text{Deike}}Bo) = 3.1 \times 10^4$] and Bo $= 1$ appears to be an outlier as our prediction for this point deviates significantly more than the rest, but remains within the same deviation order as the points of Berny *et al.* [41] at Bo $= 1$.

To conclude this appendix, we present a comparison of the first ejected drop size and velocity in surfactant-laden cases in Figs. 12(d) and 12(e). Our numerical results are compared with experimental data from Refs. [19,20,52] for SDS surfactant across various ranges of Bo, Oh, and C/CMC. In these plots, sizes and velocities are nondimensionalized by the effective viscous length and velocity ($l_{\text{vis,eff}}$ and $u_{\text{vis,eff}}$, respectively), calculated using Eq. (A1) with the system's surface tension at the initial surfactant concentration. ϕ_{eff} and La$_{\text{eff}}$ are similarly computed. As evidenced in other applications involving surfactants, the presence of these contaminants typically results in reduced droplet sizes in liquid-air and liquid-liquid systems [36]. This is clearly illustrated in Fig. 12(d), where the dimensionless drop sizes from all referenced studies, including our numerical analysis, fall well below the scaling laws for uncontaminated systems, with only a few exceptions observed in Ref. [20]. It is important to note that our displayed computational points correspond to those cases where the full postcollapse dynamics were simulated and jet pinch-off was observed.

Figure 12(e) compares the reported values of the first detached drop velocity from the aforementioned references with those from our study, as well as with Deike *et al.*'s [4] scaling for clean interfaces. Our data are presented both in terms of the velocity at the instant preceding detachment and the jet ejection velocity, in accordance with Ref. [8] (see inverted triangles and triangles, respectively, in the figure). Considering the results and discussion in Sec. III C (Fig. 10), our data in Fig. 12 suggest that the jet ejection velocity in surfactant-laden systems exceeds the clean interface scaling and its associated uncertainty (approximately 20%). Interestingly, the opposite trend is observed for drop detachment velocity, indicating significant Marangoni-driven effects that oppose jet growth, as thoroughly Analyzed in Ref. [16].

APPENDIX B: ENERGY ANALYSIS IN CLEAN INTERFACES

In this appendix we provide an additional view of the influence of non-negligible gravitational effects in uncontaminated interfaces, as explored in the main text in Sec. III A. We base this exploration of clean interfaces on the energy work conducted in Ref. [21] on bursting bubbles in viscoplastic media.

Figure 13 presents the temporal evolution of kinetic energy, denoted as $E_k = \int_V (\rho \mathbf{u}^2) \, dV$, interfacial area normalized by the initial value, $A_{s,0}$, viscous dissipation energy, $E_\mu = \int_t (\epsilon_\mu) dt$ [66], and maximal vertical interface location, $\tilde{z}_{\max}$, for various Bo; ϵ_μ is calculated as $\epsilon_\mu = \int_V (2\mu |\mathbf{D}|^2) dV$, where $|\mathbf{D}|$ is the second invariant of the deformation tensor. Here, E_k and E_μ are normalized by $\sigma_s R_0^2$, and we take a flat liquid pool as a reference state to calculate the excess A_s due to the cavity. The notably faster interfacial energy loss with respect to the system's initial energy (i.e., $A_{s,0}$) for larger Bo [see Fig. 13(b)], combined with their lower energy dissipated by viscous forces at the same Oh, and their lower maximal and asymptotic $\tilde{E}_k$ values, suggest a heightened presence of gravitational potential energy (E_p, with the liquid pool-atmosphere interface as the reference position), retarding wave motion ($E_p \sim$ Bo [21]) in the precollapse stages. As previously elucidated,
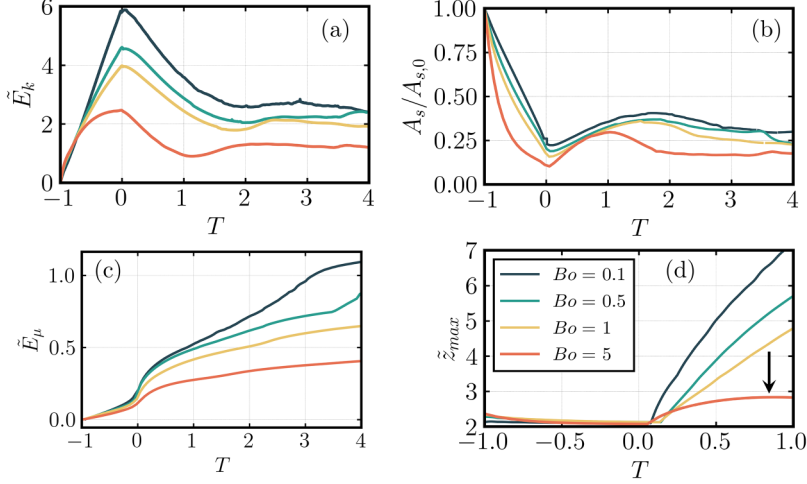
FIG. 13. Temporal evolution of kinetic energy, interfacial area, viscous dissipation energy, and maximal vertical location of the interface in surfactant-free cases (i.e., vertical position of the Worthington jet or released drops for $(\tilde{t} - \tilde{t}_0)/\tilde{t}_0 > 0$). The jet characterized by Bo = 5 did not produce drops, as indicated by the black arrow. For all cases in this figure, Oh = 3.21×10^{-3}.

these effects are present during the rise of the Worthington jet [see Fig. 13(d)], bringing about significantly shorter jets and entirely precluding pinch-off for Bo = 5.

APPENDIX C: CAP RETRACTION AND ITS EFFECTS ON EJECTED JETS

As briefly mentioned at the end of Sec. III A, cap retraction dynamics are increasingly relevant as Bo grows due to the comparable timescales associated with cap retraction and bubble collapse. In all simulations, we opted for neglecting the effects of the cap given that the time associated
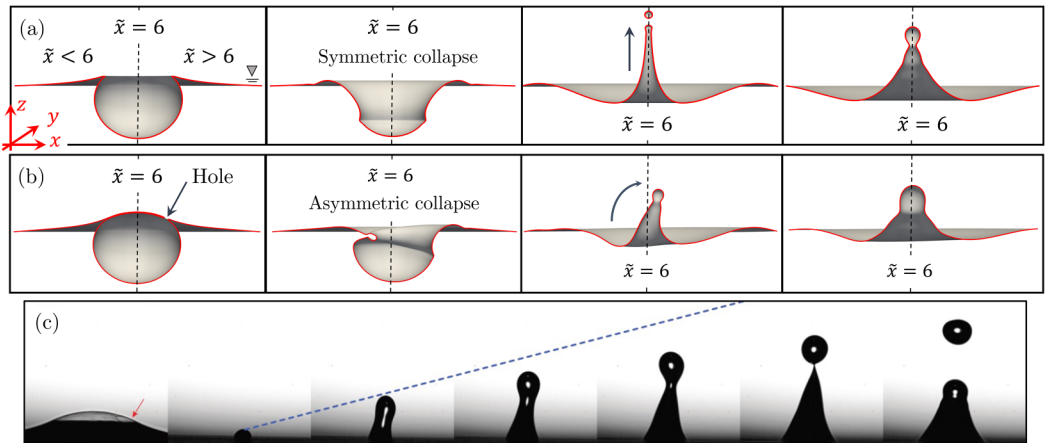

FIG. 14. Influence of bubble cap and hole opening location on a Worthington jet: (a) schematic of capless bursting, inducing a symmetric train of capillary waves along the bubble and generating a symmetric Worthington jet; (b) schematic of asymmetric bursting, generating an oblique jet. The simulation conditions of (a) and (b) correspond to Bo = 0.5 and Oh = 1×10^{-2} with cap thickness $\delta = 0.05 R_0$; (c) experimental images of asymmetric bursting taken and adapted from Ref. [67].

with its retraction is typically at least two to three orders of magnitude lower than those of cavity collapse. Nevertheless, we highlight in this appendix that an asymmetric puncture in the cap can have enormous consequences in the pre- and postcollapse dynamics. As depicted in Figs. 14(a) and 14(b), a hole opening in the $\tilde{x} > 6$ region brings about the generation of an oblique jet due to the dominant capillary waves focusing at a point shifted away from $\tilde{x} = 6$. These phenomena have been observed experimentally in the work of Ref. [67], showcased in Fig. 14(c).

---

[1] E. Ghabache and T. Séon, Size of the top jet drop produced by bubble bursting, Phys. Rev. Fluids **1**, 051901 (2016).

[2] T. Séon and G. Liger-Belair, Effervescence in champagne and sparkling wines: From bubble bursting to droplet evaporation, Eur. Phys. J. Spec. Top. **226**, 117 (2017).

[3] F. Veron, Ocean spray, Annu. Rev. Fluid Mech. **47**, 507 (2015).

[4] L. Deike, E. Ghabache, G. Liger-Belair, A. K. Das, S. Zaleski, S. Popinet, and T. Séon, Dynamics of jets produced by bursting bubbles, Phys. Rev. Fluids **3**, 013603 (2018).

[5] H. Lhuissier and E. Villermaux, Bursting bubble aerosols, J. Fluid Mech. **696**, 5 (2012).

[6] E. Villermaux, X. Wang, and L. Deike, Bubbles spray aerosols: Certitudes and mysteries, PNAS Nexus **1**, pgac261 (2022).

[7] X. Yu, H. Gu, S. Gupta, Q. Ma, L. Cheng, Y. Zhou, and H. Liang, Bubble floatation, burst, drainage, and droplet release characteristics on a free surface: A review, Phys. Fluids **35**, 041302 (2023).

[8] J. M. Gordillo and J. Rodríguez-Rodríguez, Capillary waves control the ejection of bubble bursting jets, J. Fluid Mech. **867**, 556 (2019).

[9] J. M. Gordillo and F. J. Blanco-Rodríguez, Theory of the jets ejected after the inertial collapse of cavities with applications to bubble bursting jets, Phys. Rev. Fluids **8**, 073606 (2023).

[10] F. J. Blanco-Rodríguez and J. M. Gordillo, On the jets produced by drops impacting a deep liquid pool and by bursting bubbles, J. Fluid Mech. **916**, A37 (2021).

[11] C. F. Brasz, C. T. Bartlett, P. L. L. Walls, E. G. Flynn, Y. E. Yu, and J. C. Bird, Minimum size for the top jet drop from a bursting bubble, Phys. Rev. Fluids **3**, 074001 (2018).

[12] L. Duchemin, S. Popinet, C. Josserand, and S. Zaleski, Jet formation in bubbles bursting at a free surface, Phys. Fluids **14**, 3000 (2002).

[13] A. M. Gañán-Calvo, Revision of bubble bursting: Universal scaling laws of top jet drop size and speed, Phys. Rev. Lett. **119**, 204502 (2017).

[14] C. Y. Lai, J. Eggers, and L. Deike, Bubble bursting: Universal cavity and jet profiles, Phys. Rev. Lett. **121**, 144501 (2018).

[15] P. L. L. Walls, L. Henaux, and J. C. Bird, Jet drops from bursting bubbles: How gravity and viscosity couple to inhibit droplet production, Phys. Rev. E **92**, 021002 (2015).

[16] C. R. Constante-Amores, L. Kahouadji, A. Batchvarov, S. Shin, J. Chergui, D. Juric, and O. K. Matar, Dynamics of a surfactant-laden bubble bursting through an interface, J. Fluid Mech. **911**, A57 (2021).

[17] B. Ji, Z. Yang, Z. Wang, R. H. Ewoldt, and J. Feng, Secondary bubble entrainment via primary bubble bursting at a viscoelastic surface, Phys. Rev. Lett. **131**, 104002 (2023).

[18] B. Néel, M. A. Erinin, and L. Deike, Role of contamination in optimal droplet production by collective bubble bursting, Geophys. Res. Lett. **49**, e2021GL096740 (2022).

[19] J. Pierre, M. Poujol, and T. Séon, Influence of surfactant concentration on drop production by bubble bursting, Phys. Rev. Fluids **7**, 073602 (2022).

[20] E. J. Vega and J. M. Montanero, Influence of a surfactant on bubble bursting, Exp. Therm. Fluid Sci. **151**, 111097 (2024).

[21] V. Sanjay, D. Lohse, and M. Jalaal, Bursting bubble in a viscoplastic medium, J. Fluid Mech. **922**, A2 (2021).

[22] S. Shin and D. Juric, A hybrid interface method for three-dimensional multiphase flows based on front tracking and level set techniques, Int. J. Numer. Methods Fluids **60**, 753 (2009).

[23] S. Shin, J. Chergui, and D. Juric, A solver for massively parallel direct numerical simulation of three-dimensional multiphase flows, J. Mech. Sci. Technol. **31**, 1739 (2017).

[24] S. Shin, J. Chergui, D. Juric, L. Kahouadji, O. K. Matar, and R. V. Craster, A hybrid interface tracking–level set technique for multiphase flow with soluble surfactant, J. Comput. Phys. **359**, 409 (2018).

[25] C. D. Eggleton and K. J. Stebe, An adsorption–desorption-controlled surfactant on a deforming droplet, J. Colloid Interface Sci. **208**, 68 (1998).

[26] M. Muradoglu and G. Tryggvason, Simulations of soluble surfactants in 3D multiphase flow, J. Comput. Phys. **274**, 737 (2014).

[27] H. Manikantan and T. M. Squires, Surfactant dynamics: Hidden variables controlling fluid flows, J. Fluid Mech. **892**, P1 (2020).

[28] U. Olgac and M. Muradoglu, Effects of surfactant on liquid film thickness in the Bretherton problem, Int. J. Multiphase Flow **48**, 58 (2013).

[29] S. Tasoglu, U. Demirci, and M. Muradoglu, The effect of soluble surfactant on the transient motion of a buoyancy-driven bubble, Phys. Fluids **20**, 040805 (2008).

[30] C. R. Constante-Amores, A. Batchvarov, L. Kahouadji, S. Shin, J. Chergui, D. Juric, and O. K. Matar, Role of surfactant-induced Marangoni stresses in drop-interface coalescence, J. Fluid Mech. **925**, A15 (2021).

[31] C. R. Constante-Amores, L. Kahouadji, A. Batchvarov, S. Shin, J. Chergui, D. Juric, and O. K. Matar, Dynamics of retracting surfactant-laden ligaments at intermediate Ohnesorge number, Phys. Rev. Fluids **5**, 084007 (2020).

[32] C. R. Constante-Amores, T. Abadie, L. Kahouadji, S. Shin, J. Chergui, D. Juric, A. A. Castrejón-Pita, and O. K. Matar, Direct numerical simulations of turbulent jets: Vortex-interface-surfactant interactions, J. Fluid Mech. **955**, A42 (2023).

[33] M. Kalli, P. Pico, L. Chagot, L. Kahouadji, S. Shin, J. Chergui, D. Juric, O. K. Matar, and P. Angeli, Effect of surfactants during drop formation in a microfluidic channel: A combined experimental and computational fluid dynamics approach, J. Fluid Mech. **961**, A15 (2023).

[34] A. Batchvarov, L. Kahouadji, C. R. Constante-Amores, G. F. Noroes Gonçalves, S. Shin, J. Chergui, D. Juric, R. V. Craster, and O. K. Matar, Three-dimensional dynamics of falling films in the presence of insoluble surfactants, J. Fluid Mech. **906**, A16 (2020).

[35] A. Batchvarov, L. Kahouadji, M. Magnini, C. R. Constante-Amores, S. Shin, J. Chergui, D. Juric, R. V. Craster, and O. K. Matar, Effect of surfactant on elongated bubbles in capillary tubes at high Reynolds number, Phys. Rev. Fluids **5**, 093605 (2020).

[36] P. Pico, L. Kahouadji, S. Shin, J. Chergui, D. Juric, and O. K. Matar, Drop encapsulation and bubble bursting in surfactant-laden flows in capillary channels, Phys. Rev. Fluids **9**, 034001 (2024).

[37] C. W. Shu and S. Oshert, Efficient implementation of essentially non-oscillatory shock-capturing schemes, II, J. Comput. Phys. **83**, 32 (1989).

[38] Y. X. Wang and J. M. Wen, Gear method for solving differential equations of gear systems, J. Phys.: Conf. Ser. **48**, 143 (2006).

[39] S. Shin and D. Juric, Modeling three-dimensional multiphase flow using a level contour reconstruction method for front tracking without connectivity, J. Comput. Phys. **180**, 427 (2002).

[40] C. S. Peskin, Numerical analysis of blood flow in the heart, J. Comput. Phys. **25**, 220 (1977).

[41] A. Berny, L. Deike, T. Séon, and S. Popinet, Role of all jet drops in mass transfer from bursting bubbles, Phys. Rev. Fluids **5**, 033605 (2020).

[42] H. Zhang and Q. Liu, Numerical investigation on performance of moisture separator by Lagrangian-Eulerian strategy: Physical mechanisms, theoretical models, and advanced algorithms, Ann. Nucl. Energy **137**, 107081 (2020).

[43] K. J. Stebe, S.-Y. Lin, and C. Maldarelli, Remobilizing surfactant retarded fluid particle interfaces. I. Stress-free conditions at the interfaces of micellar solutions of surfactants with fast sorption kinetics, Phys. Fluids **3**, 3 (1991).

[44] H. C. Mayer and R. Krechetnikov, Landau-Levich flow visualization: Revealing the flow topology responsible for the film thickening phenomena, Phys. Fluids **24**, 052103 (2012).

[45] E. Ghabache, A. Antkowiak, C. Josserand, and T. Séon, On the physics of fizziness: How bubble bursting controls droplets ejection, Phys. Fluids **26**, 121701 (2014).

[46] B. W. Zeff, B. Kleber, J. Fineberg, and D. P. Lathrop, Singularity dynamics in curvature collapse and jet eruption on a fluid surface, Nature (London) **403**, 401 (2000).

[47] B. Ji, A. Singh, and J. Feng, Water-to-air transfer of nano/microsized particulates: Enrichment effect in bubble bursting jet drops, Nano Lett. **22**, 5626 (2022).

[48] M. A. Erinin, C. Liu, X. Liu, W. Mostert, L. Deike, and J. H. Duncan, The effects of surfactants on plunging breakers, J. Fluid Mech. **972**, R5 (2023).

[49] R. V. Craster, O. K. Matar, and D. T. Papageorgiou, Pinchoff and satellite formation in compound viscous threads, Phys. Fluids **15**, 3409 (2003).

[50] E. Antonopoulou, O. G. Harlen, M. Rump, T. Segers, and M. A. Walkley, Effect of surfactants on jet break-up in drop-on-demand inkjet printing, Phys. Fluids **33**, 072112 (2021).

[51] C. R. Constante-Amores, L. Kahouadji, S. Shin, J. Chergui, D. Juric, J. R. Castrejón-Pita, O. K. Matar, and A. A. Castrejón-Pita, Impact of droplets onto surfactant-laden thin liquid films, J. Fluid Mech. **961**, A8 (2023).

[52] B. Néel and L. Deike, Collective bursting of free-surface bubbles, and the role of surface contamination, J. Fluid Mech. **917**, A46 (2021).

[53] M. Kalli and P. Angeli, Effect of surfactants on drop formation flow patterns in a flow-focusing microchannel, Chem. Eng. Sci. **253**, 117517 (2022).

[54] B. Ambravaneswaran and O. A. Basaran, Effects of insoluble surfactants on the nonlinear deformation and breakup of stretching liquid bridges, Phys. Fluids **11**, 997 (1999).

[55] P. M. Kamat, B. W. Wagoner, S. S. Thete, and O. A. Basaran, Role of Marangoni stress during breakup of surfactant-covered liquid threads: Reduced rates of thinning and microthread cascades, Phys. Rev. Fluids **3**, 043602 (2018).

[56] P. M. Kamat, B. W. Wagoner, Alfonso A. Castrejón-Pita, J. R. Castrejón-Pita, C. R. Anthony, and O. A. Basaran, Surfactant-driven escape from endpinching during contraction of nearly inviscid filaments, J. Fluid Mech. **899**, A28 (2020).

[57] N. M. Kovalchuk and M. J. H. Simmons, Effect of soluble surfactant on regime transitions at drop formation, Colloids Surf. A **545**, 1 (2018).

[58] Y. C Liao, E. I. Franses, and O. A. Basaran, Deformation and breakup of a stretching liquid bridge covered with an insoluble surfactant monolayer, Phys. Fluids **18**, 022101 (2006).

[59] P. T. McGough and O. A. Basaran, Repeated formation of fluid threads in breakup of a surfactant-covered jet, Phys. Rev. Lett. **96**, 054502 (2006).

[60] L. Dubitsky, O. McRae, and J. C. Bird, Enrichment of scavenged particles in jet drops determined by bubble size and particle position, Phys. Rev. Lett. **130**, 054001 (2023).

[61] D. C. Blanchard and L. D. Syzdek, Concentration of bacteria in jet drops from bursting bubbles, J. Geophys. Res. **77**, 5087 (1972).

[62] H. F. Bezdek and A. F. Carlucci, Surface concentration of marine bacteria, Limnol. Oceanogr. **17**, 566 (1972).

[63] S. Krishnan, E. J. Hopfinger, and B. A. Puthenveettil, On the scaling of jetting from bubble collapse at a liquid surface, J. Fluid Mech. **822**, 791 (2017).

[64] D. E. Spiel, On the births of jet drops from bubbles bursting on water surfaces, J. Geophys. Res. **100**, 4995 (1995).

[65] D. E. Spiel, More on the births of jet drops from bubbles bursting on seawater surfaces, J. Geophys. Res. Oceans **102**, 5815 (1997).

[66] O. Ramírez-Soto, V. Sanjay, D. Lohse, J. T. Pham, and D. Vollmer, Lifting a sessile oil drop from a superamphiphobic surface with an impacting one, Sci. Adv. **6**, 34 (2020).

[67] G. Élisabeth, Surface libre hors équilibre: De l'effondrement de cavité aux jets étirés, Ph.D. thesis, Université Pierre et Marie Curie Paris 6, Paris (2015).